The Astrophysical Journal Supplement Series, 208:25 (33pp), 2013 October doi:10.1088/0067-0049/208/2/25

MULTIBAND DIAGNOSTICS OF UNIDENTIFIED 1FGL SOURCES WITH *SUZAKU* AND *SWIFT* X-RAY OBSERVATIONS

Y. Takeuchi, J. Kataoka[1], K. Maeda[1], Y. Takahashi[1], T. Nakamori[2], and M. Tahara[1]
[1] Research Institute for Science and Engineering, Waseda University, 3-4-1 Okubo, Shinjuku, Tokyo 169-8555, Japan; uto_of_take@suou.waseda.jp
[2] Department of Physics, Faculty of Science, Yamagata University, 1-4-12 Kojirakawa, Yamagata, Yamagata 990-8560, Japan
Received 2013 May 15; accepted 2013 July 16; published 2013 September 30

ABSTRACT

We have analyzed all the archival X-ray data of 134 unidentified (unID) gamma-ray sources listed in the first *Fermi*/LAT (1FGL) catalog and subsequently followed up by the *Swift*/XRT. We constructed the spectral energy distributions (SEDs) from radio to gamma-rays for each X-ray source detected, and tried to pick up unique objects that display anomalous spectral signatures. In these analyses, we target all the 1FGL unID sources, using updated data from the second *Fermi*/LAT (2FGL) catalog on the Large Area Telescope (LAT) position and spectra. We found several potentially interesting objects, particularly three sources, 1FGL J0022.2−1850, 1FGL J0038.0+1236, and 1FGL J0157.0−5259, which were then more deeply observed with *Suzaku* as a part of an AO-7 program in 2012. We successfully detected an X-ray counterpart for each source whose X-ray spectra were well fitted by a single power-law function. The positional coincidence with a bright radio counterpart (currently identified as an active galactic nucleus, AGN) in the 2FGL error circles suggests these sources are definitely the X-ray emission from the same AGN, but their SEDs show a wide variety of behavior. In particular, the SED of 1FGL J0038.0+1236 is not easily explained by conventional emission models of blazars. The source 1FGL J0022.2−1850 may be in a transition state between a low-frequency peaked and a high-frequency peaked BL Lac object, and 1FGL J0157.0−5259 could be a rare kind of extreme blazar. We discuss the possible nature of these three sources observed with *Suzaku*, together with the X-ray identification results and SEDs of all 134 sources observed with the *Swift*/XRT.

Key words: galaxies: active – gamma rays: general – radiation mechanisms: general – X-rays: general

Online-only material: color figures, machine-readable tables

1. INTRODUCTION

Since the successful launch of the *Fermi Gamma-ray Space Telescope* in 2008 June, we have had the opportunity to study gamma-ray emission from different types of high-energy sources with much improved sensitivity and localization capabilities than with the EGRET instrument on board the *Compton Gamma-Ray Observatory*. With the field of view (FoV) covering 20% of the sky at every moment (five times larger than EGRET), and its improved sensitivity (by more than an order of magnitude with respect to EGRET), the Large Area Telescope (LAT; Atwood et al. 2009) aboard *Fermi* surveys the entire sky each day down to photon flux levels of $F_{>100\,\mathrm{MeV}} \simeq$ few $\times\ 10^{-7}$ photons cm^{-2} s^{-1}. The number of detected gamma-ray sources has increased, with the second *Fermi*/LAT Catalog (2FGL; Nolan et al. 2012) containing 1873 gamma-ray sources in the 100 MeV to 100 GeV range, while 271 objects were previously listed in the third EGRET Catalog (3EG; Hartman et al. 1999). More than 1000 gamma-ray sources included in the 2FGL are proposed to be associated with active galactic nuclei (AGNs) and 87 sources with pulsars (PSRs; Abdo et al. 2010a), including 21 millisecond pulsars (MSPs). Other associations have included supernova remnants (Abdo et al. 2010d), low-mass/high-mass X-ray binaries (Abdo et al. 2009), pulsar wind nebulae (Abdo et al. 2010e), normal and starburst galaxies (Abdo et al. 2010c), and the giant lobes of a radio galaxy (Abdo et al. 2010f).

However, no obvious counterparts at longer wavelengths have been found for as much as 31% of the 2FGL *Fermi*/LAT objects so that several hundreds of GeV sources currently remain unassociated with any known astrophysical systems. In other words, the nature of unassociated gamma-ray sources is still one of the major puzzles in astrophysics; the mystery has not yet been solved. Fortunately, the improved localization capabilities of the *Fermi*/LAT (typical 95% confidence radii $r_{95} \sim 0.^{\circ}1$–$0.^{\circ}2$, and even $0.^{\circ}005$–$0.^{\circ}01$ for the brightest sources; Nolan et al. 2012), when compared to that of EGRET (typical $r_{95} \sim 0.^{\circ}4$–$0.^{\circ}7$), enables more effective follow-up studies at radio, optical, and X-ray frequencies, which can help to unravel the nature of the unidentified (unID) gamma-ray emitters. Indeed, for example, a lot of *Fermi* sources were identified using *Wide Field Infrared Survey Explorer* (*WISE*) infrared (IR) data (D'Abrusco et al. 2013; Massaro et al. 2013).

In this context, we started a new project to investigate the nature of unID *Fermi*/LAT objects through X-ray follow-up observations with the XIS sensor on board the *Suzaku* X-ray satellite (see Section 2). For example, the results of the first-year campaign conducted in *Suzaku* AO-4 (2009) were presented in Maeda et al. (2011). In this campaign, the X-ray counterpart for one of the brightest unassociated *Fermi*/LAT objects, 1FGL J1231.1−1410 (also detected by EGRET as 3EG J1234−1318 and EGR J1231−1412), was discovered for the first time. The X-ray spectrum was well fitted by a blackbody with an additional power-law component, supporting the recent identification of this source with an MSP. In the second-year campaign (AO-5), another seven unID *Fermi*/LAT sources were subsequently observed with *Suzaku* (Takahashi et al. 2012). In particular, this paper presented a convenient method of classifying the objects into "AGN-like" and "PSR-like" sources by comparing their multiwavelength properties with those of known AGNs and pulsars. In the third year (AO-6), 1FGL J2339.7−0531 (Y. Yatsu et al. 2013 in preparation; also Romani & Shaw 2011) and 1FGL J1311.7−3429 (Romani 2012; Kataoka et al. 2012) were intensively monitored with a

total exposure time of 200 ks. Both sources are now suggested to be "black widow" MSP systems and have been newly categorized as "radio-quiet" MSPs. As these projects show, X-ray follow-up observations, especially those using *Suzaku*, provided various fruitful results to clarify the nature of unassociated gamma-ray sources, and were able to find a new type of gamma-ray emitter.

To complete the series of X-ray follow-up programs described above, we further carried out the analysis of all the archival X-ray data of 134 unID gamma-ray sources in the first *Fermi*/LAT (1FGL) catalog of point sources (Abdo et al. 2010b) with the *Swift*/XRT. Note that all 134 sources have been detected in the 2FGL catalog, hence updated data on their LAT position and spectra available from the 2FGL catalog are used throughout this work. This allowed us to construct the spectral energy distributions (SEDs) of each object from radio to gamma-rays (see Section 2 and the Appendix) for the first time. Note that we target all the 1FGL unID sources that satisfy our selections (see Section 2), using updated/improved information from the 2FGL catalog on their LAT positions and spectra in this paper. Moreover, three sources that displayed potentially interesting SEDs, 1FGL J0022.2−1850 (or 2FGL J0022.2−1853), 1FGL J0038.0+1236 (or 2FGL J0037.8+1238), and 1FGL J0157.0−5259 (or 2FGL J0157.2−5259), were deeply observed with *Suzaku* as part of the AO-7 campaign in 2012. In the 2FGL catalog, both 1FGL J0022.2−1850 and 1FGL J0157.0−5259 are categorized as active galaxies of uncertain type (agu), while 1FGL J0038.0+1236 was classified as a BL Lac type of blazar (bzb) based on the positional coincidences to sources observed at another wavelength. As we discuss later, the unique SEDs of these three objects do not coincide with those of conventional blazars. In Section 2, we describe the analysis of the 134 1FGL unID sources with *Swift*. Subsequently, in Section 3, deep *Suzaku* follow-up observations of the three selected sources, 1FGL J0022.2−1850, 1FGL J0038.0+1236, and 1FGL J0157.0−5259, are shown. The results of the analysis are given in Section 4. The discussion and summary are presented in Sections 5 and 6, respectively.

2. *SWIFT* ANALYSIS OF 134 1FGL unID SOURCES

2.1. Observation and Data Reduction

Swift (Geherels et al. 2004) is a gamma-ray observatory launched on 2004 November 20. The primary goal of this mission is to explore and follow-up on gamma-ray bursts, but high mobility and sensitivity to localized sources, especially using the X-Ray Telescope (XRT; Burrows et al. 2005) and UVOT (Roming et al. 2005), also make it viable for follow-up of unID gamma-ray objects discovered by *Fermi*/LAT. In fact, *Swift* follow-up observations have aided in the study of many unID *Fermi*/LAT sources (Cognard et al. 2011; Keith et al. 2011; Ransom et al. 2011; Theureau et al. 2011; Cheung et al. 2012; Kong et al. 2012). Here we tried to perform a systematic and uniform analysis of unID gamma-ray sources observed thus far with *Swift* using archival data. The selection criteria are given as follows: (1) categorized as unID sources in 1FGL catalog, (2) localized at high Galactic latitude $|b| > 10^{\circ}$, (3) observational data were made public by October 2011, and (4) the positional center of the *Swift* FoV is within 12 arcmin from the 1FGL sources. Among 630 unID sources listed in the 1FGL catalog, this selection yielded 134 sources which we analyzed here. In the reduction and analysis of the *Swift*/XRT and UVOT data, HEADAS software version 6.11 and the most recent calibration databases (CALDB) as of 2011 October 20 were used. We did not use Burst Alert Telescope (BAT) data because most sources are not bright enough to be detected within BAT's short exposure times of typically 10 ks or less. In the XRT analysis, we used only the PC mode data, while only image data taken from photometry observations were used in the UVOT analysis.

2.2. XRT Analysis

Two types of XRT archival data can be obtained from the *Swift* Data Center: Level 1 and 2. Level 2 cleaned data have gone through the standard pipeline process; however, we calibrated the Level 1 data ourselves in a way recommended by the *Swift* team.[3] Particularly, we selected the good time interval (GTI) from the Level 1 data using `xrtpipeline`. In this process, we changed only the default `xrtpipeline` selection in the CCD temperature range of "$\leqq -47$" to "$\leqq -50$," where the former is the default value. In the XRT image analysis, we tried to detect the X-ray counterparts of 1FGL unID sources, and to localize each source. First, we extracted X-ray images in the energy range 0.3–10 keV using `xselect`. Next, using `ximage`, we searched for "possible" X-ray sources with $>3\sigma$ confidence level in photon statistics against the background. The positions of these sources were determined with a typical accuracy of $\sim 5''$ using `xrtcentroid`. The results of our X-ray source detection are listed in Table 6 (see the Appendix). In the Appendix, we also show the XRT images corresponding to each of the 134 1FGL unID gamma-ray sources indicating the 2FGL error ellipses (Figure 11). In these images, bright radio sources and X-ray sources listed in the *ROSAT* All-Sky Survey Bright Source Catalogue (Voges et al. 1999) corresponding to the XRT sources are also plotted as magenta crosses. Finally, if the X-ray sources were detected within the 2FGL 95% position error ellipse, we performed X-ray spectral analysis for those sources. We note that very bright X-ray sources with more than 0.6 counts s^{-1} should cause serious pile-up effects in the XRT CCD, however, there were no such bright sources in our analyzed sample.

In the XRT spectral analysis, PHA files were extracted from event files with `xselect` and exposure maps were made using `xrtexpomap`. We made auxiliary response files (ARFs) using `xrtmkarf` and used the current redistribution matrix files (RMFs) in CALDB. We extracted photons from circles with 30 arcsec radii around the source positions as the source regions, and we set the concentric rings centered at the source positions with radii of 30–180 arcsec as the background regions. In cases where some background sources appeared in the field, or overall regions could not be fitted in the CCD, we simply removed the region surrounding these background sources or the region outside the CCD chip. If there was no source detected above 3σ inside the 2FGL error ellipse, we derived the upper limit assuming the 2FGL error ellipses as the source region of corresponding X-ray flux. The results of spectral analysis are included in the SEDs given in the Appendix. We note that X-ray spectral data were binned in two different ways according to source brightness: (1) they were binned with `grppha` so that at least 20 photons were included in each bin, (2) the X-ray spectral data (0.5–10.0 keV) were divided logarithmically into five bins. When a source had more than 40 counts, we used method (1); otherwise we used method (2).

[3] The SWIFT XRT Data Reduction Guide: http://heasarc.nasa.gov/docs/swift/analysis/xrt_swguide_v1_2.pdf.

Table 1
Suzaku XIS Observation Logs

Target Name	R.A. (deg)	Decl. (deg)	Exposure (ks)	Obs. Start (UT)
1FGL J0022.2−1850	5.5540	−18.9060	34.2	2012 May 30 12:57:00
1FGL J0038.0+1236	9.4627	12.6391	18.8	2012 Jun 29 23:56:00
1FGL J0157.0−5259	29.3640	−53.0280	12.1	2012 May 28 16:19:00

2.3. UVOT Analysis

We performed an analysis of UVOT data only when the X-ray counterpart of the 1FGL source was found in the *Swift*/XRT FoV. *Swift*/UVOT archival data have six types of filters (v, b, u, $uvw1$, $uvw2$, and $uvm2$), with each filter providing different wavelength data. When each filter included more than one observation, the images and exposure maps were summed using `uvotimsum`. Using `uvotdetect`, we detected sources with high signal-to-noise ratios ($>3\sigma$). We set the circles around those sources with a radius of 5 arcsec as the source regions if any source was found in the 90% error ellipse of the *Swift*/XRT source. Then, circles with a radius of 30″ as the background regions were taken from the area where no sources were found. Finally, we obtained the magnitude of each filter using `uvotsource`. Corrections for Galactic extinction were performed following the method described in Cardelli et al. (1998).

2.4. Multiwavelength Analysis

To construct SEDs of each 1FGL source, we used not only the *Swift*/XRT and *Swift*/UVOT flux data analyzed in this paper but also gamma-ray fluxes listed in the 2FGL catalog, and radio fluxes mostly from the NED database and W3Browse based on a variety of catalogs. We searched for radio counterparts associated with the XRT or UVOT objects mentioned above in the HEASARC/Master Radio Catalog,[4] which includes the NRAO VLA Sky Survey (NVSS; Condon et al. 1998, 1.4 GHz), the FIRST Survey Catalog of 1.4 GHz Radio Sources (White et al. 1997, 1.4 GHz), Sydney University Molonglo Sky Survey Source Catalog (SUMSS; Mauch et al. 2003, 843 MHz), VLA Low-Frequency Sky Survey Discrete Source Catalog (Cohen et al. 2007, 74 MHz), the Westerbork in the Southern Hemisphere Survey (De Breuck et al. 2002), the Australia Telescope 20 GHz Survey Catalog (Murphy et al. 2010), the Green Bank 6 cm Catalog of Radio Sources (Gregory et al. 1996), and Parkes-MIT-NRAO Southern, Tropical, Equatorial, and Zenith Survey (Wright et al. 1996) and those radio fluxes are added in the SEDs. Note that if no corresponding radio sources were found in the 2FGL 95% error ellipses, we obtained the upper limit from the brightest radio source in the error ellipse. Likewise, if no source was found in the error ellipse but some sources were found outside of the region, we used the sensitivity limits of those sources as an upper limit. Finally, resultant SEDs and flux values of each wavelength are given in the Appendix (Figure 12 and Tables 5 and 6).

3. *SUZAKU* ANALYSIS OF THREE 1FGL unID SOURCES

3.1. Observation and Data Reduction

We observed three *Fermi*/LAT objects that exhibited potentially interesting or anomalous SEDs (which are difficult to explain using standard emission models of blazars, i.e., synchrotron self-Compton (SSC) or external Compton models as explained in Fossati et al. 1998) with the *Suzaku* X-ray astronomy satellite (Mitsuba et al. 2007). These were denoted in the 1FGL catalog as 1FGL J0022.2−1850, 1FGL J0038.0+1236, and 1FGL J0157.0−5259, and in the 2FGL catalog as 2FGL J0022.2−1853, 2FGL J0037.8+1238, and 2FGL J0157.2−5259, respectively. The *Suzaku* observation logs are summarized in Table 1. The observations were performed with XIS which consists of four CCD cameras each placed in the focal plane of the XRT (Serlemitsos et al. 2007), and with the Hard X-ray Detector (HXD) which consists of Si PIN photo-diodes (HXD-PIN) and GSO scintillation counters (HXD-GSO; Kokubun et al. 2007; Takahashi et al. 2007).

One of the XIS sensors (XIS 1) has a back-illuminated CCD, while the other three (XISs 0, 2, and 3) utilize front-illuminated (FI) CCDs. However, because of an anomaly in 2006 November, the operation of XIS2 was terminated. Hence, here we use only the three remaining CCDs. The XIS was operated in the normal full-frame clocking mode with the 3×3 or 5×5 editing mode. We analyzed the screened XIS data, reduced using *Suzaku* software version 1.2. The screening was based on the following criteria: (1) only *ASCA*-grade 0, 2, 3, 4, 6 events were accumulated, while hot and flickering pixels were removed from the XIS image using the `sisclean` script (Day et al. 1998), (2) the time interval after the passage of the South Atlantic Anomaly was greater than 60 s, and (3) the object was at least 5° and 20° above the rim of the Earth (ELV) during night and day, respectively. In addition, we also selected the data with a cutoff rigidity larger than 6 GV. In the reduction and analysis of the *Suzaku* XIS data, HEADAS software version 6.12 and a CALDB released on 2009 September 25 were used. The XIS cleaned event data-set was obtained in the combined 3×3 and 5×5 edit modes using `xselect`.

The HXD data were also processed in a standard way as follows. First, we obtained the appropriate version 2.0 "tuned" non-X-ray background file (NXB) for this observation. Because the HXD background file has a time variation, we made a new GTI file to match the GTI between observation data and NXB data using `mgtime`. Next, using this new GTI file, we generated time-averaged HXD spectra with `xselect`. These were then dead-time-corrected using `hxddtcor` script. Epoch-appropriate response files for XIS-nominal pointing were downloaded from the *Suzaku* CALDB Web site. The contribution from the Cosmic X-ray Background (CXB) was simulated following a recipe provided by the HXD team.[5]

3.2. Image Analysis

We extracted the XIS images within the photon energy range 0.4–10 keV from only the two FI CCDs (XIS 0, XIS 3). In the image analysis, we excluded calibration sources at the corner of the CCD chips. The images of the NXB were obtained from the night Earth data using `xisnxbgen` (Tawa et al. 2008). Since

[4] http://heasarc.nasa.gov/W3Browse/all/radio.html

[5] See http://heasarc.gsfc.nasa.gov/docs/suzaku/analysis/pin_cxb.html.

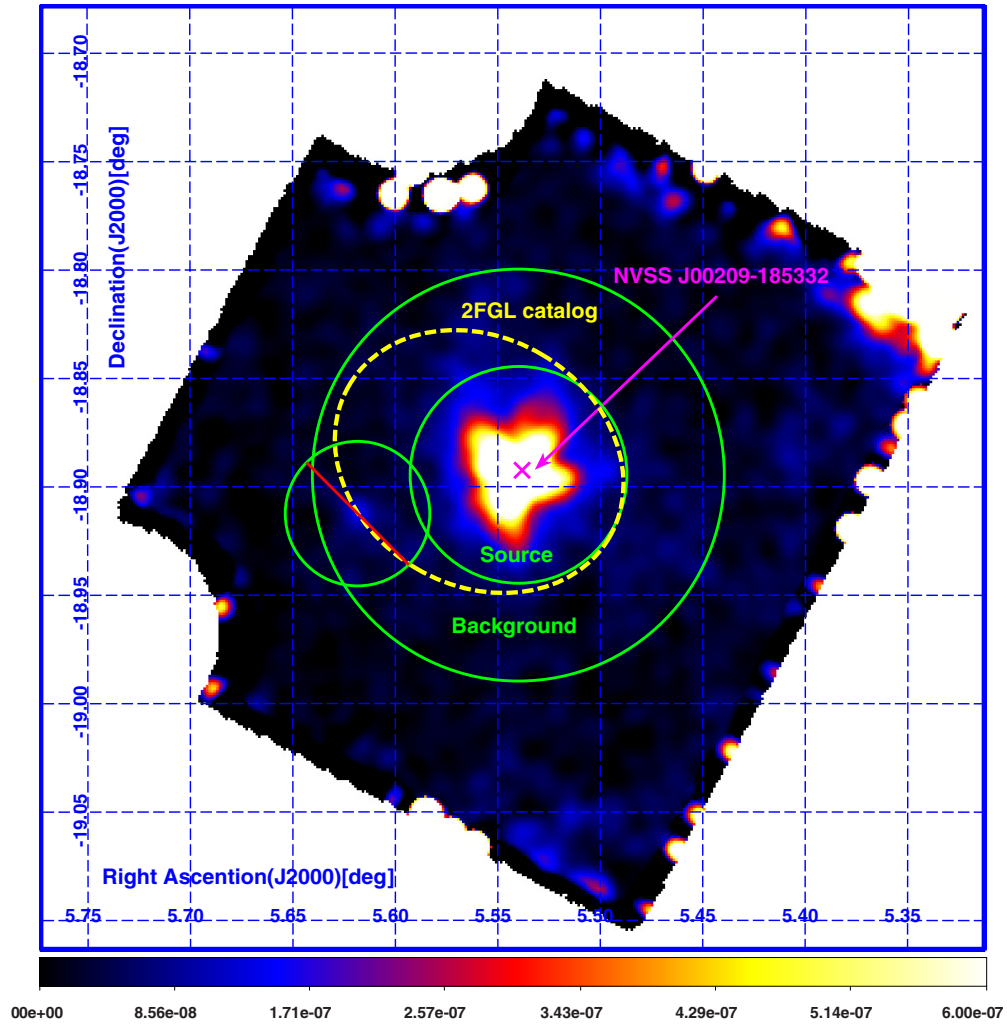

Figure 1. *Suzaku* X-ray image of 1FGL J0022.2-1850 (vignetting and exposure corrections applied). Data from XIS 0 and XIS 3 are summed in the 0.4–10 keV energy band. The magenta cross denotes the position of the radio counterpart source NVSS J00209−185332, the yellow dotted ellipse denotes the 95% position error of 2FGL J0022.2−1853, and the inner green ellipse denotes the *Suzaku* source extraction region. The outer green ellipse without an inner source region denotes the *Suzaku* background extraction region.

(A color version of this figure is available in the online journal.)

the exposure times for the original data were different from that of NXB, we calculated the appropriate exposure-corrected original and NXB maps using `xisexpmapgen` (Ishisaki et al. 2007). The corrected NXB images were next subtracted from the corrected original images. In addition, we simulated flat sky images using `xissim` (Ishisaki et al. 2007), and applied a vignetting correction. All the images obtained with XIS0 and XIS3 were combined and re-binned by a factor of 4 (CCD pixel size 24 μm × 24 μm, so that 1024 × 1024 pixels cover an 18′ × 18′ region on the sky; Koyama et al. 2007). Throughout these processes, we performed vignetting correction for all the images. Finally, the images were smoothed with a Gaussian function with $\sigma = 0'.24$. Note that the apparent features at the edges of these exposure-corrected images are undoubtedly spurious due to low exposure in those regions.

3.3. Spectral Analysis

In the spectral analysis of XIS, we analyzed the three target sources as point sources based on the result of our image analysis (see Section 5). Source regions for spectral analysis indicated by inner green circles were selected around each detected X-ray source within the error ellipse of a gamma-ray emitter. The corresponding background regions were indicated by the outer green ellipse after the removal of source regions. Moreover, if X-ray sources other than the target source were found, we excluded the region around those sources from the spectral analysis region. We extracted the spectra from each source region using `xselect` for each CCD (XIS 0, XIS 1, XIS 3). Next, we made RMFs and ARFs using `xisrmfgen` and `xissimarfgen` (Ishisaki et al. 2007), respectively. In addition, we used the new contamination files ae_xi0_contami_20120711.fits, ae_xi1_contami_20120711.fits, and ae_xi3_contami_20120711.fits,[6] because the response function of XIS0 is imperfect for recent observations. Using these RMFs and ARFs, the corrected spectrum about the energy response and the effective area of the XIS were obtained. Finally, spectral analysis and model fitting were performed with `xspec` version 12.7.0. In the spectral analysis of the HXD, we also subtracted the NXB and CXB to obtain the HXD-PIN spectrum, then we performed model fitting together with the XIS spectrum.

[6] See http://byakko.scphys.kyoto-u.ac.jp:31415/xis/XIS_Suzaku/2012_MeetRep/20120711_wada_CALDB/.

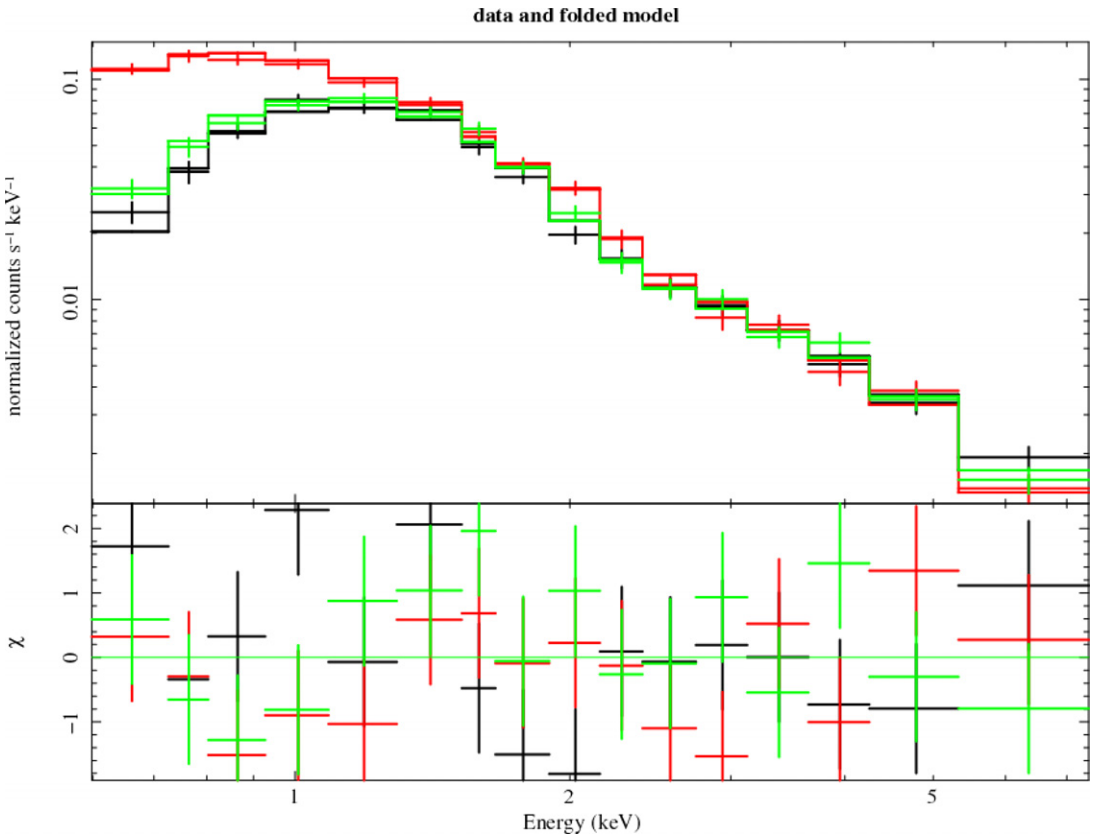

Figure 2. *Suzaku* XIS spectra of 1FGL J0022.2−1850 in the photon energy range 0.4–10 keV, fitted by the model `wabs + power-law`. Spectra of XIS0, XIS1, and XIS3 are shown in black, red, and green, respectively.

(A color version of this figure is available in the online journal.)

Table 2
Radio Counterpart Sources for Each Target

Target Name	R.A. (deg)	Decl. (deg)	$F_{1.4\,\mathrm{GHz}}$ (mJy)	$F_{843\,\mathrm{MHz}}$ (mJy)
NVSS J00209−185332	5.5381667	−18.892444	22.1 ± 0.8	···
NVSS J003750+123818	9.461875	12.638556	75.1 ± 2.3	···
SUMSS J015657−530157	29.240833	−53.032778	···	43.4 ± 1.5

4. RESULTS OF *SUZAKU* OBSERVATIONS

We show in this section the results of X-ray image and spectral analysis for each object observed with *Suzaku*. Since we did not detect any time-variability for each source in *Suzaku* exposures, the results of the timing analysis are not given in this paper. We successfully detected significant signals from the X-ray counterpart of 1FGL J0157.0-5259 with HXD/PIN, but below the sensitivity limit of the HXD/GSO, while the other two sources were too faint to be detected with either HXD/PIN or GSO. Therefore, as for the HXD analysis of 1FGL J0157.0−5259 in this paper, we use only the data from HXD/PIN.

4.1. 1FGL J0022.2−1850

In our *Suzaku* observations, we detected one X-ray point source (R.A., decl.) = (5.°540, −18.°894) within the updated 2FGL error ellipse corresponding to 1FGL J0022.2−1850. Figure 1 shows the corresponding X-ray image of 1FGL J0022.2−1850 as described in Section 4.1. The radio source NVSS J003750+123818 appears to be the counterpart of 1FGL J0022.2−1850, as indicated by the magenta cross at the center of this X-ray source (see Section 5). Moreover, one unknown point source is detected within the background region for spectral analysis (because the central source is very bright, it is difficult to see this source in Figure 1).

In Figure 2, the X-ray spectrum of the *Suzaku* source, which we argue is the most likely counterpart of 1FGL J0022.2−1850, is shown. The XIS spectra is given for the energy range 0.6–7.5 keV. In the spectral analysis, the target X-ray source is so bright that we selected a source region assuming 3′ radii (a typical half-power diameter of the XRT is 2′; Serlemitsos et al. 2007). Meanwhile, we excluded one contaminating field X-ray point source detected by *Suzaku*, assuming the source region 2′ radii from the source and background regions for spectral analysis described in Section 4.2. The spectrum is well fitted by a single power-law continuum with a photon index, $\Gamma = 2.43 \pm 0.03$, moderated by Galactic absorption only. The Galactic hydrogen column density was fixed as $N_{\mathrm{H}} = 2.02 \times 10^{20}$ cm^{-2} (Dickey & Lockman 1990). The value of $\chi^2/\mathrm{dof} = 46.81/46$ indicated that this is a satisfactory model for 1FGL J0022.2−1850. The details of the fitting results are summarized in Table 2.

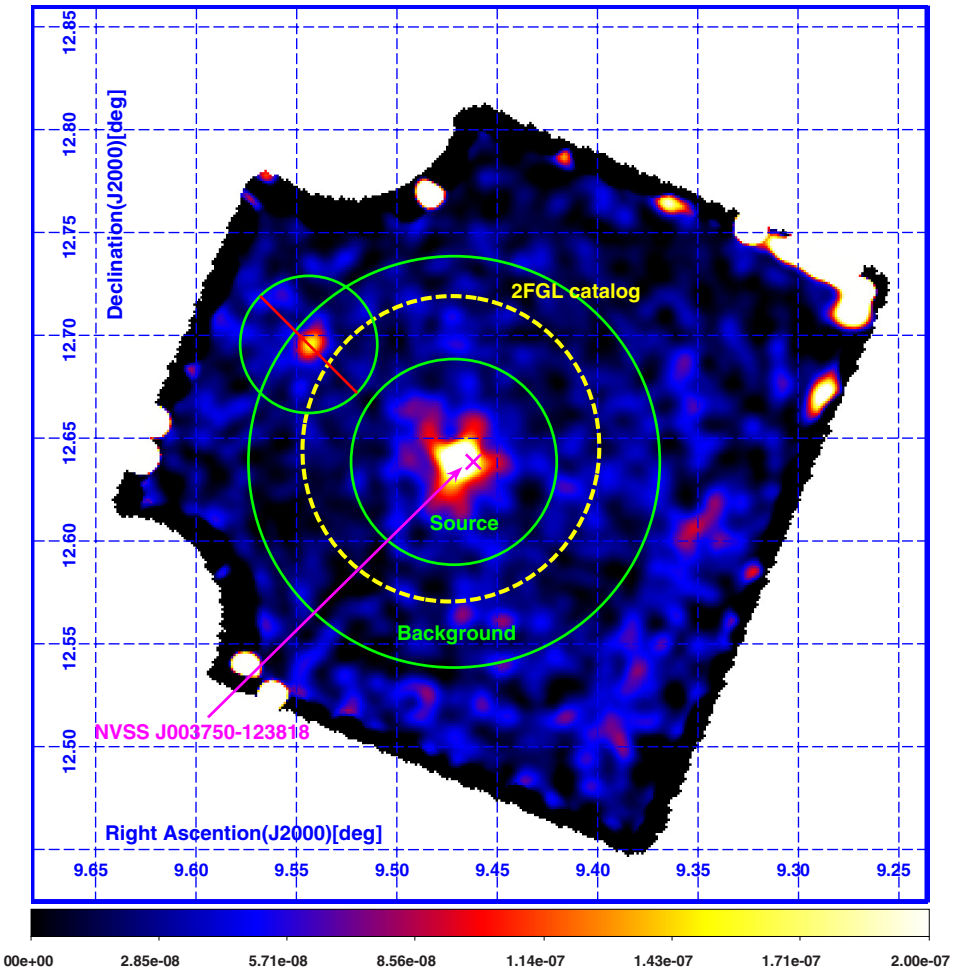

Figure 3. Same as Figure 1, but for the target source 1FGL J0038.0+1236 and radio counterpart NVSS J003750+123818.
(A color version of this figure is available in the online journal.)

Table 3
Fitting Parameters for Each *Suzaku* Target (The Power-law Model)

Target Name	$N_{\rm H}$ ($\rm cm^{-2}$)	Γ	χ^2/dof	$P(\chi^2)$	$F_{0.6-7.5\,\rm keV}$ ($\rm erg\ cm^{-2}\ s^{-1}$)
1FGL J0022.2−1850	2.02×10^{20} (fixed)	2.43 ± 0.03	46.81/46	4.39×10^{-1}	2.12×10^{-12}
1FGL J0038.0+1236	5.38×10^{20} (fixed)	2.76 ± 0.17	85.54/70	9.98×10^{-2}	2.11×10^{-13}
1FGL J0157.0−5259	2.70×10^{20} (fixed)	$1.85 \pm 6.66 \times 10^{-3}$	3184.74/2757	1.95×10^{-8}	3.21×10^{-11}

4.2. 1FGL J0038.0+1236

One X-ray point source (R.A., decl.) = (9.°472, 12.°639) was found with *Suzaku* within the improved 2FGL error ellipse corresponding to 1FGL J0038.0+1236. The corresponding X-ray image made via the method described in Section 4.1 is shown in Figure 3. Moreover, one unknown point source is detected within the background region for spectral analysis. The radio source, NVSS J00209−185332 (shown by the magenta cross; see Section 6), is coincident with the X-ray position and we propose that this is the most likely counterpart of 1FGL J0038.0+1236.

Figure 4 shows the X-ray spectrum of the point source detected by *Suzaku* near the center of the 2FGL error ellipse of 1FGL J0038.0+1236 (0.6–7.5 keV). The source region was selected with 3′ radii because the target source is too bright to cover the entire region of the emission from the target source with 2′ radii. When we selected the background region, the region from the X-ray contaminant source was excluded with 2′ radii in order to avoid subtracting too much as background. The spectrum could be well fitted by a single power-law continuum with $\Gamma = 2.76 \pm 0.17$, moderated by Galactic absorption only. The Galactic hydrogen column density was fixed as $N_{\rm H} = 5.38 \times 10^{20}\ \rm cm^{-2}$ (Dickey & Lockman 1990). The value of χ^2/dof = 85.54/70 indicates that this is a satisfactory model for 1FGL J0038.0+1236. The details of the fitting results are summarized in Table 3.

4.3. 1FGL J0157.0−5259

We succeeded in detecting a bright X-ray point source with *Suzaku* within the 2FGL error ellipse corresponding to 1FGL J0157.0−5259. Figure 5 shows the corresponding X-ray image (see Section 4.1). The X-ray source is located at (R.A., decl.) = (29.°253, −53.°035), as shown in Figure 5. The position of the radio source, SUMSS J015657−530157, is shown by a magenta cross (see Section 5). In this observation, we did

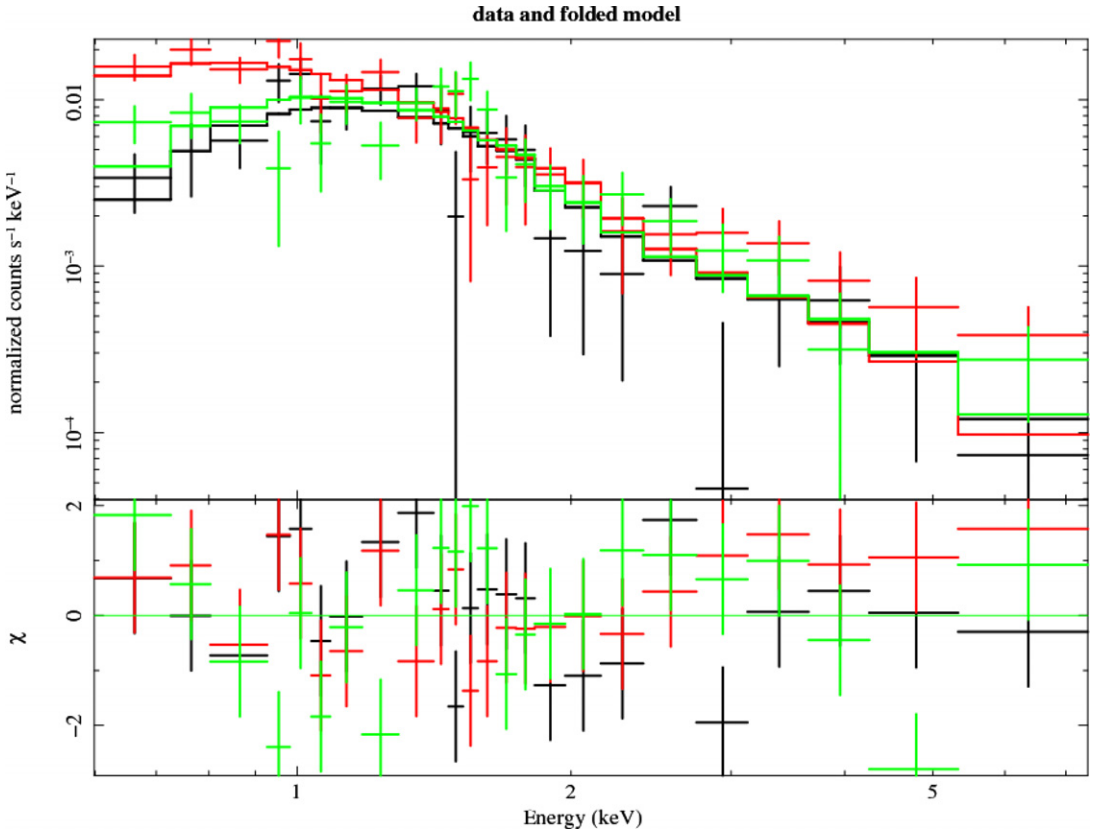

Figure 4. *Suzaku* XIS spectra of 1FGL J0038.0+1236 in the photon energy range 0.4–10 keV, fitted by the model `wabs + power-law`. Spectra of XIS0, XIS1, and XIS3 are shown in black, red, and green, respectively.

(A color version of this figure is available in the online journal.)

Table 4
Swift/XRT Results for 1FGL Objects

1FGL Src	XRT Src No.	R.A. (J2000) (deg)	Decl. (J2000) (deg)	$r_{90\%}$ ($''$)	Count Rates (1E−03 counts s^{-1})	S/N
1FGL J0001.9–4158	1	0.3864	−41.9227	3.73	6.95E+01 ± 3.6	19.5
	2	0.3671	−42.0492	6.31	2.22 ± 7.3E−01	3.0
	3	0.2813	−41.8854	5.70	3.36 ± 9.2E−01	3.7
1FGL J0009.1 + 5031	1	2.3453	50.5071	4.90	1.00E+01 ± 1.6	6.2
	2	2.3150	50.5960	5.64	3.05 ± 9.3E−01	3.3
	3	2.1369	50.5176	6.31	2.62+/−8.8E−01	3.0
	4	2.4958	50.6476	6.41	3.16 ± 1.0	3.0
	5	2.0160	50.4936	6.12	3.39 ± 1.1	3.1
	6	1.9824	50.6048	7.09	4.18 ± 1.3	3.2

Notes. This table only shows the details of high signal-to-noise (3σ) sources detected within the *Swift*/XRT FoV. The radii of 90% confidence error circles are described by $r_{90\%}$. Count rates are shown in the energy range of 0.3–10 keV.

(This table is available in its entirety in a machine-readable form in the online journal. A portion is shown here for guidance regarding its form and content.)

not find any other contamination source as in the above two observations.

The X-ray spectrum (XIS + HXD) of the *Suzaku* source, which we propose is the most likely counterpart of 1FGL J0157.0−5259, is shown in Figure 6 within the energy range 0.6–40.0 keV (XIS 0.4–10.0 keV, HXD 15.0–40.0 keV). In this spectral analysis, we set the extraction region with a radius of $4'$ to encircle this bright source. On the other hand, we set the background region with a larger radius, and the location of the center of the background region displaced from the center of target source so that it is not over the region covered by the CCD. The spectrum could be well fitted by a single power-law continuum with $\Gamma = 1.85 \pm 0.01$, moderated by Galactic absorption only. The Galactic hydrogen column density was fixed as $N_{\rm H} = 2.70 \times 10^{20}$ cm^{-2} (Dickey & Lockman 1990). The value of χ^2/dof = 3184.74/2757 indicates that this is a satisfactory model for 1FGL J0157.0−5259. The details of the fitting results are summarized in Table 4.

5. DISCUSSION

In the uniform analysis of archival *Swift* data, we found several objects that seemed to display anomalous SEDs atypical of AGNs or PSRs. Then we performed *Suzaku* X-ray follow-up observations of three such sources to more accurately determine

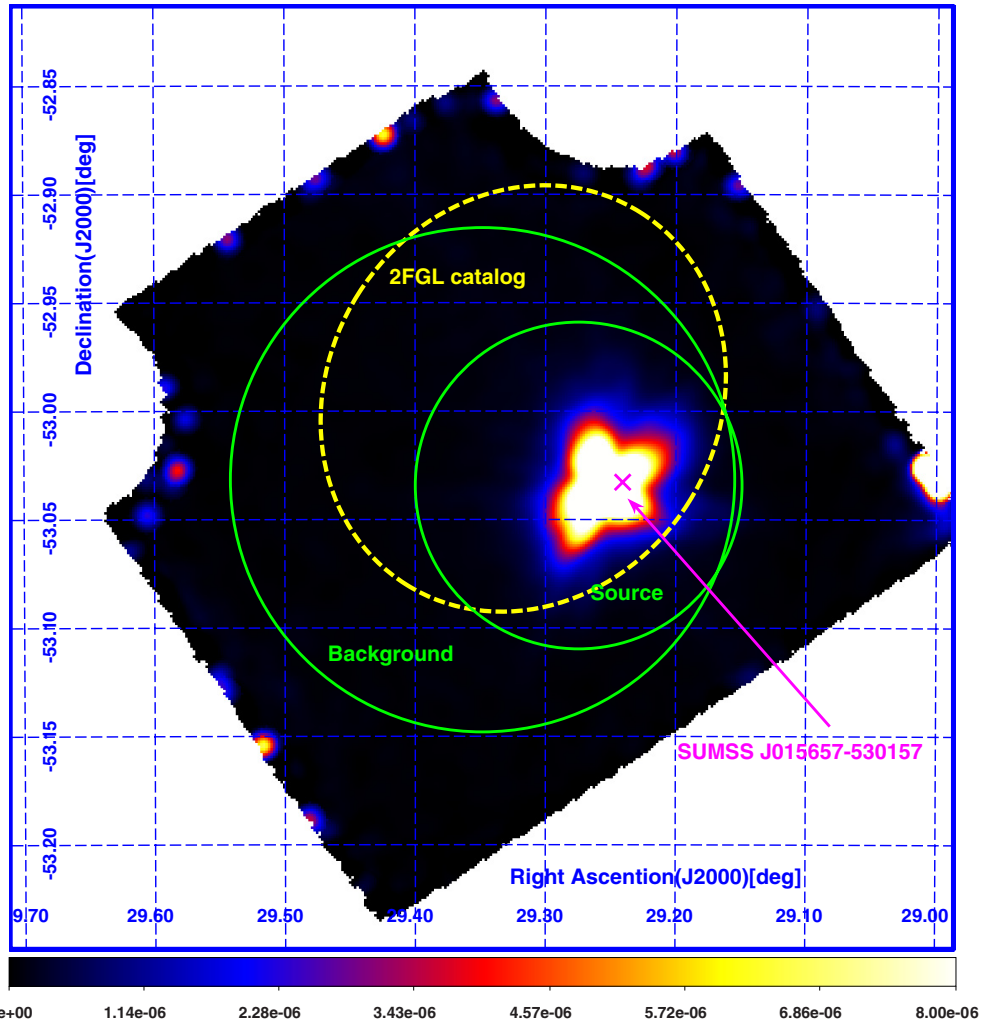

Figure 5. Same as Figure 1, but for the target source 1FGL J0157.0−5259 and radio counterpart SUMSS J015657−530157.
(A color version of this figure is available in the online journal.)

the SEDs of each object (Figures 7–9). Different fluxes between *Swift*/XRT and *Suzaku*/*XIS* seen in these SEDs indicate that these objects should have a temporal variability that was not seen within the individual shorter *Suzaku* exposures. Moreover, thanks to the good sensitivity and long exposure of the *Suzaku* data, we have additional hints to reveal the nature of each source as discussed below.

An X-ray source found within the updated 2FGL error ellipse of 1FGL J0022.2−1850 is positionally consistent with the radio source NVSS J00209−185332 found in the NVSS catalog (Condon et al. 1998; see Table 2). Moreover, an IR counterpart source WISE J002209.25−185334.7 located at (R.A., decl.) = (5.°5385563, −18.°8929772) was found in the *WISE* All-Sky Release (Wright et al. 2010). The SED of 1FGL J0022.2−1850/WISE J002209.25−185334.7/NVSS J00209−185332, as well as our *Suzaku*/XIS data and derived XRT and UVOT fluxes from *Swift*, are shown in Figure 7. From the relatively high radio flux and flat X-ray spectrum obtained with *Swift*/XRT, this object is likely to be a low-frequency peaked BL Lac (LBL). However, during our *Suzaku* observation, the X-ray spectrum was observed to be substantially steeper, more typical of a high-frequency peaked BL Lac (HBL). Moreover, the flat GeV gamma-ray spectrum is typical of HBLs like Mrk 421 and Mrk 501, rather than an LBL. Considering the Cherenkov Telescope Array which is an initiative to build a next generation observatory for very high energy gamma-rays will have an improved sensitivity by an order of magnitude with respect to current instruments ($\sim 10^{-14}$ erg cm^{-2} s^{-1} above a few TeV), the upward shape of the *Fermi*/LAT spectrum suggests the source could also be detected in TeV energy in the near future.

In the case of 1FGL J0038.0+1236, the location of an X-ray counterpart discovered in our *Suzaku* observations is consistent with NVSS J003750+123818 as described as in Table 2, and the optical counterpart SDSS J003750.88+123819.9 (classified as GALAXY) located at (R.A., decl.) = (9.°462, 12.°638875) and IR counterpart WISE J003750.87+123819.9 located at (R.A., decl.) = (9.°4619958, 12.°6388878), were also found in the Sloan Digital Sky Survey (SDSS; Ahn et al. 2012) and *WISE* catalogs, respectively. The constructed radio to X-ray SED together with the *Swift*/XRT, UVOT and the LAT spectrum is shown in Figure 8. Since the X-ray spectrum appears very steep, this source seems to be associated with an HBL, while the steep gamma-ray spectrum observed with *Fermi*/LAT favors an FSRQ origin for this source. While optical and ultraviolet fluxes are extremely bright, this could be due to a contribution of soft photons from the host galaxy as seen in some blazar spectra (see, e.g., the SED of Mrk 501; Kataoka et al. 1999). These results show that it is difficult to explain this source using conventional leptonic models of blazars (i.e., SSC or external Compton models).

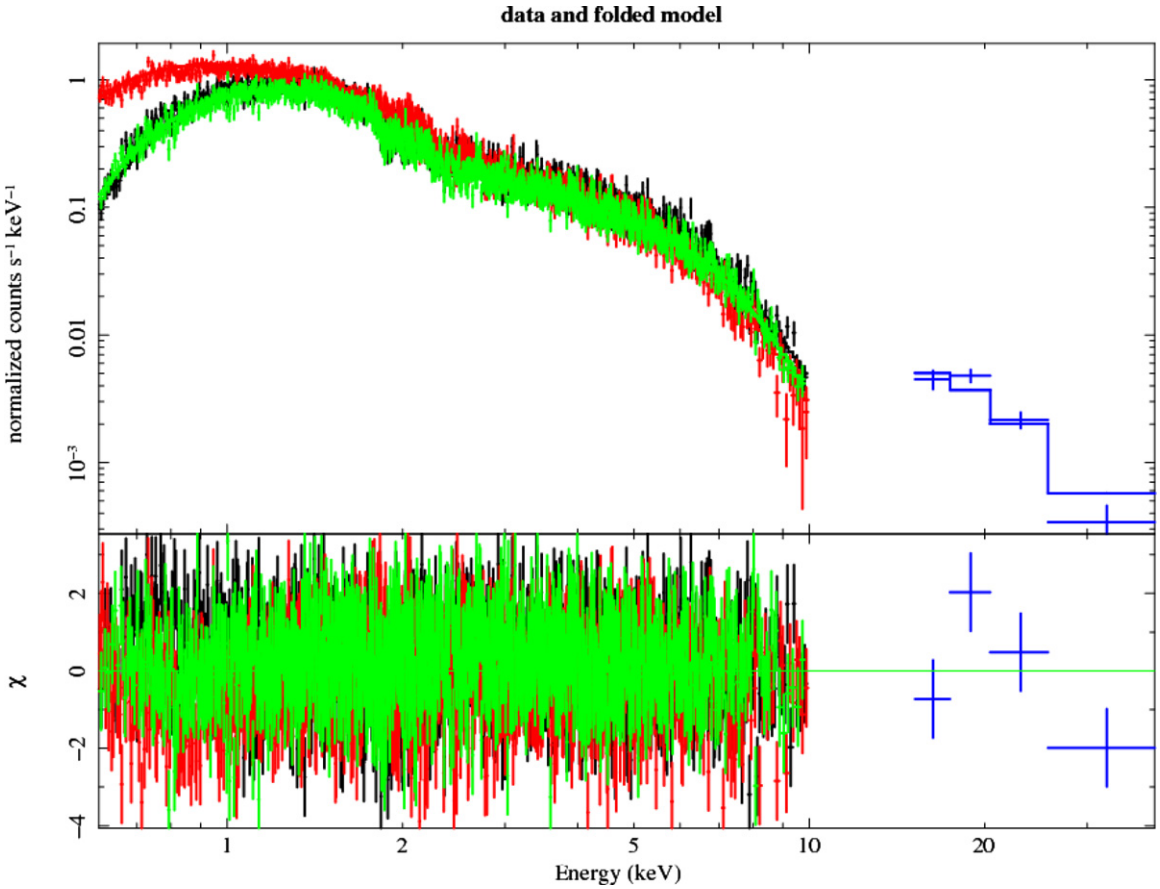

Figure 6. *Suzaku* XIS spectra of 1FGL J0157.0-5259 in the photon energy range 0.4–40 keV (XIS 0.4–10 keV, HXD 15–40 keV), fitted by the model `wabs * power-law`. Spectra of XIS0, XIS1, XIS3, and HXD are shown in black, red, green, and blue, respectively.

(A color version of this figure is available in the online journal.)

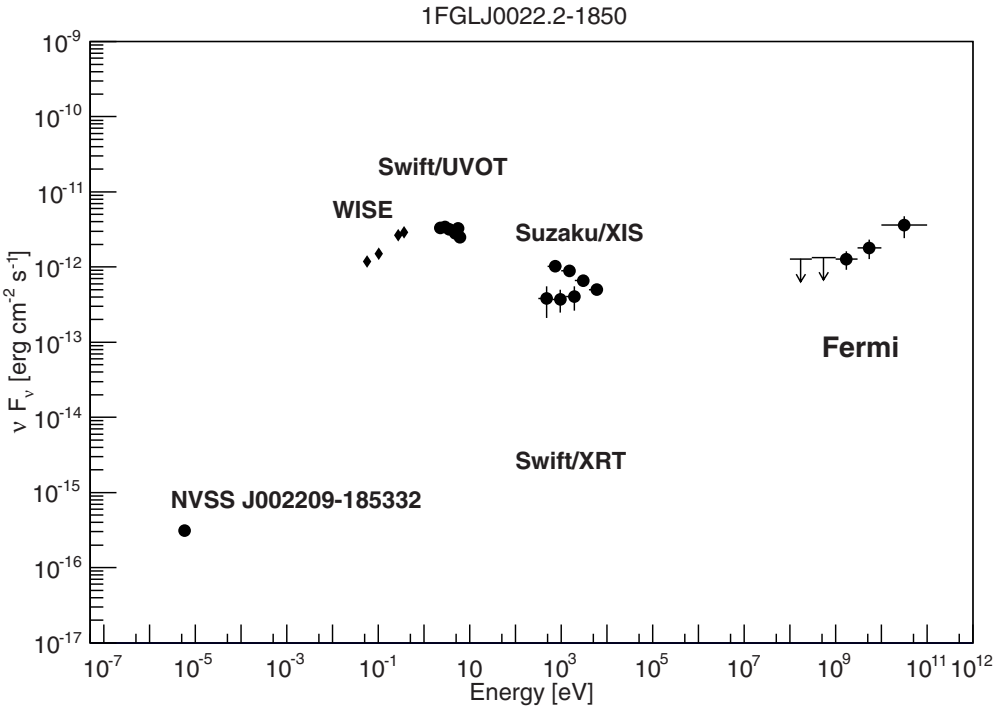

Figure 7. Broadband SEDs of 1FGL J0022.2−1850. The radio fluxes (1.4 GHz) for this source are taken from NVSS J00209−185332 as radio counterpart. The infrared fluxes (3.4 μm, 4.6 μm, 12 μm, and 22 μm) are taken from the *WISE* catalog. The optical/UV fluxes were derived from the *Swift*/UVOT observations (this work). The X-ray fluxes are taken from the *Suzaku*/XIS and *Swift*/XRT observations (this work). Finally, the gamma-ray data points are taken from the 2FGL catalog (Nolan et al. 2012).

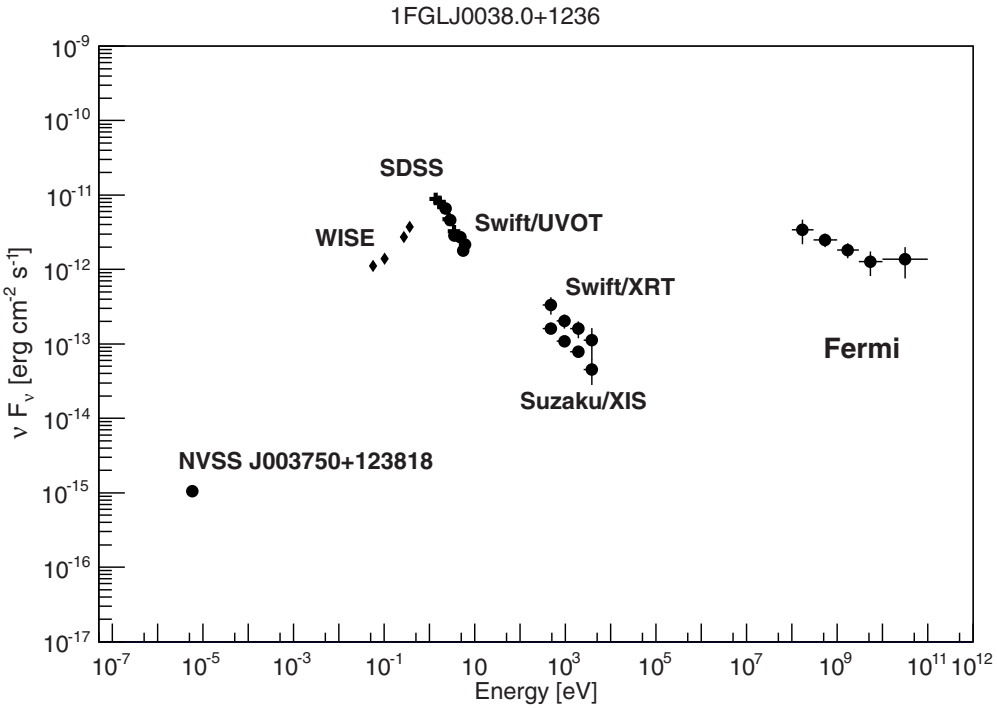

Figure 8. Broadband SEDs of 1FGL J0038.0+1236. The radio fluxes (1.4 GHz) for this source are taken from NVSS J003750*123818 as the radio counterpart. The infrared fluxes (3.4 μm, 4.6 μm, 12 μm, and 22 μm) are taken from the *WISE* catalog. The optical/UV fluxes were derived from the *Swift*/UVOT observations (this work) and the SDSS catalog. The X-ray fluxes are taken from the *Suzaku*/XIS and *Swift*/XRT observations (this work). Finally, the gamma-ray data points are taken from the 2FGL catalog (Nolan et al. 2012).

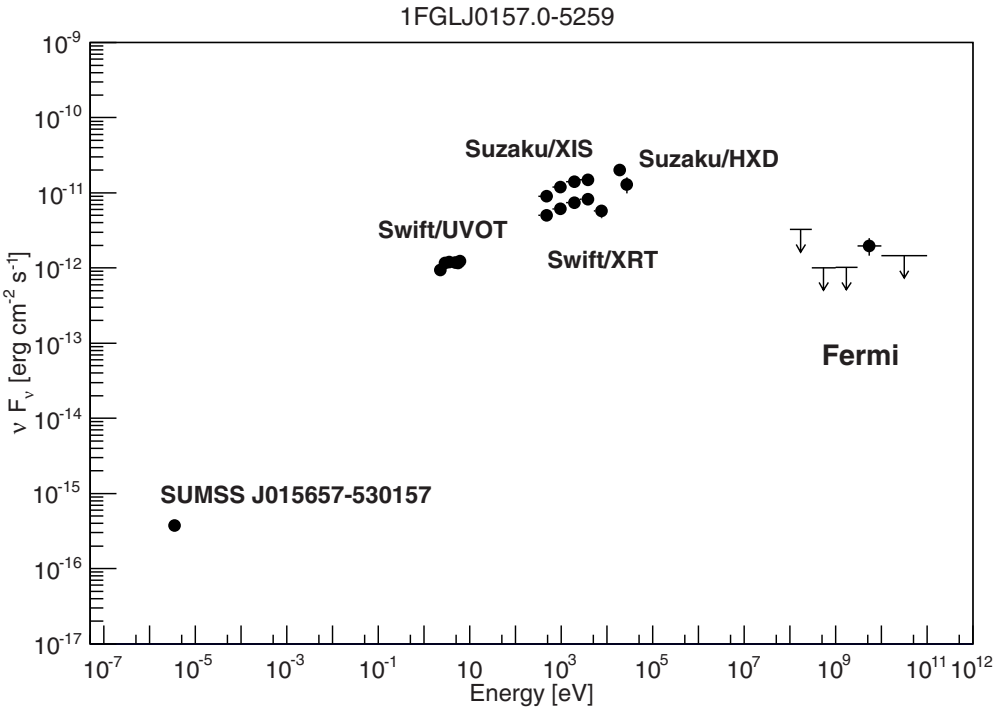

Figure 9. Broadband SEDs of 1FGL J0157.0−5259. The radio fluxes (843 MHz) for this source are taken from SUMSS J015657−530157 as the radio counterpart source. The optical/UV fluxes were derived from the *Swift*/UVOT observations. The X-ray fluxes are taken from the *Suzaku*/XIS and *Swift*/XRT observations (this work). The hard X-ray fluxes are from the *Suzaku*/HXD observations (this work). Finally, the gamma-ray data points are taken from the 2FGL catalog (Nolan et al. 2012).

In the case of 1FGL J0157.0−5259, our *Suzaku*/XIS observations revealed the presence of a quite bright X-ray counterpart in the LAT error circle, and since the hard X-ray fluxes of this source are very high, we could also obtain data from *Suzaku*/HXD. At the position of this *Suzaku* X-ray source, the radio counterpart SUMSS J015657−530157 was found in the SUMSS catalog (Mauch et al. 2003; Table 2). The broadband SED of 1FGL J0157.0−5259/SUMSS J015657−530157 along with our *Suzaku*/XIS,HXD and derived *Swift*/XRT, UVOT data are presented in Figure 9. Since the X-ray fluxes are connected

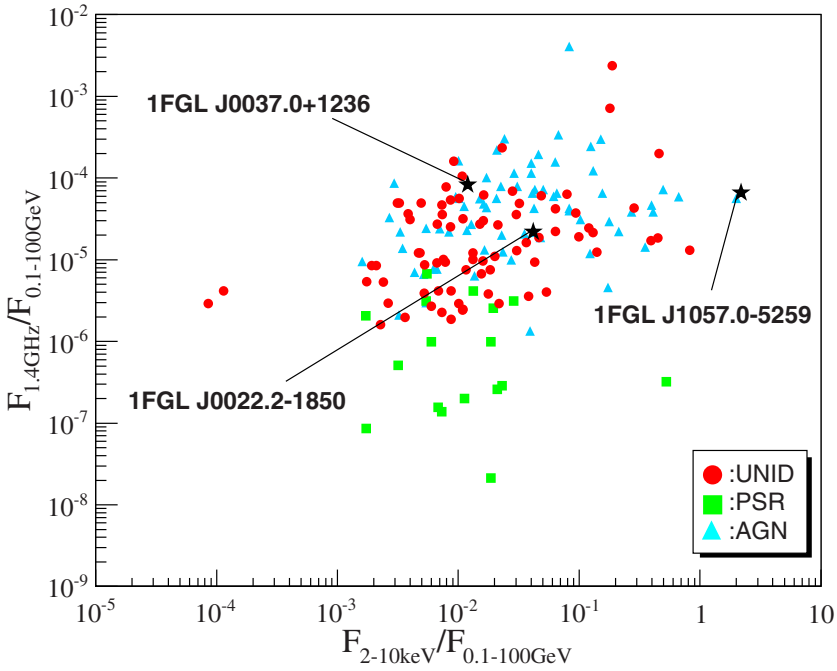

Figure 10. X-ray to gamma-ray flux ratios vs. radio to gamma-ray ratios for 1FGL 134 unID objects on which we performed follow-up observations with the *Swift*/XRT. Red circles show the flux ratios of the *Fermi*/LAT sources that are still unID in the 2FGL catalog. Aqua triangles indicate the data plots of AGNs listed in the 2FGL catalog. Green squares represent the data points of sources that are associated with PSRs listed in the 2FGL catalog. Three black stars show the target sources in this paper, 1FGL J0022.2−1850, 1FGL J0038.0+1236, and 1FGL J0157.0−5259, respectively.

(A color version of this figure is available in the online journal.)

by a straight line with the radio fluxes, these fluxes seem to be due to synchrotron radiation. The peak frequency of the synchrotron spectrum is very high (>10 keV) suggesting that the source could be a rare type of "extreme" blazar like Mrk 501 in the historical high state (Ghisellini 2004). If this source is an "extreme" blazar, observations at TeV energies or additional deep observations with *Fermi*/LAT may detect a significant signal in the future.

Finally, we made a figure similar to that described in Takahashi et al. (2012) for the 1FGL 134 unID objects in which we performed follow-up observations with *Swift*/XRT (Figure 10). This figure presents a comparison of the AGNs (aqua), PSRs (green), and unassociated sources (red) classified in the 2FGL catalog in the X-ray to gamma-ray flux ratio versus radio to gamma-ray ratio plane. The three sources we observed with *Suzaku* in this paper are shown as black stars. Apparently, these sources are situated in the typical AGN region of this diagnostic plane. It is noteworthy that 1FGL J0157.0−5259 is at the right edge of this typical AGN region, and this means the X-ray and gamma-ray flux ratios of this source are quite high, ∼2, which is consistent with our speculation that the source is an extreme HBL-type blazar.

6. SUMMARY

In this paper we reported on the results of X-ray follow-up observations of three unID gamma-ray sources detected by *Fermi*/LAT that indicate anomalous SEDs. We have successfully detected X-ray counterparts of 1FGL J0022.2−1850, 1FGL J0038.0+1236, and 1FGL J0157.0−5259 using *Suzaku*. The characteristics of each object are summarized below. We also note that these objects display temporal variability in X-rays, as indicated by the different X-ray fluxes measured by *Suzaku*/XIS and *Swift*/XRT (see Figures 7–9).

The X-ray spectrum of the discovered *Suzaku* counterpart to 1FGL J0022.2−1850 is well fitted by a single power-law model with $\Gamma = 2.43 \pm 0.03$. The spectral shape obtained with *Suzaku* (in X-rays) and *Fermi*/LAT (in gamma-rays) suggests the source is typical of an HBL-type blazar, but previous *Swift* observations show it was similar to an LBL-type blazar. The source is potentially a TeV emitter that could be detected in the near future. In the case of 1FGL J0038.0+1236, the X-ray spectrum is well fitted by a single power-law model with a photon index $\Gamma = 2.76 \pm 0.17$. At first glance, this source also seems to be classified as an HBL because the X-ray spectrum seen in Figure 8 appears very steep. However, its steep gamma-ray spectrum observed with *Fermi*/LAT favors an FSRQ origin for this source. These results show that it is difficult to explain this source using standard emission models of blazars, i.e., SSC or external Compton models. In the case of 1FGL J0157.0−5259, the *Suzaku* X-ray spectrum obtained from XIS and HXD are well fitted by a single power-law model with a photon index $\Gamma = 1.85 \pm 6.66 \times 10^{-3}$. From the multiwavelength analysis shown in Figure 9, the peak frequency of the synchrotron spectrum is very high (∼10 keV) suggesting that the source could be an "extreme" blazar like Mrk 501 in the historical high state.

We would like to thank C. C. Cheung for useful comments that helped to improve the organization of the manuscript.

APPENDIX

SWIFT OBSERVED 1FGL unID SOURCES

The XRT images corresponding to each of the 134 1FGL unID gamma-ray sources also indicating the 2FGL error ellipses are shown in Figure 11. Finally, resultant SEDs and flux values of each wavelength are given in Figure 12 and Tables 5 and 6.

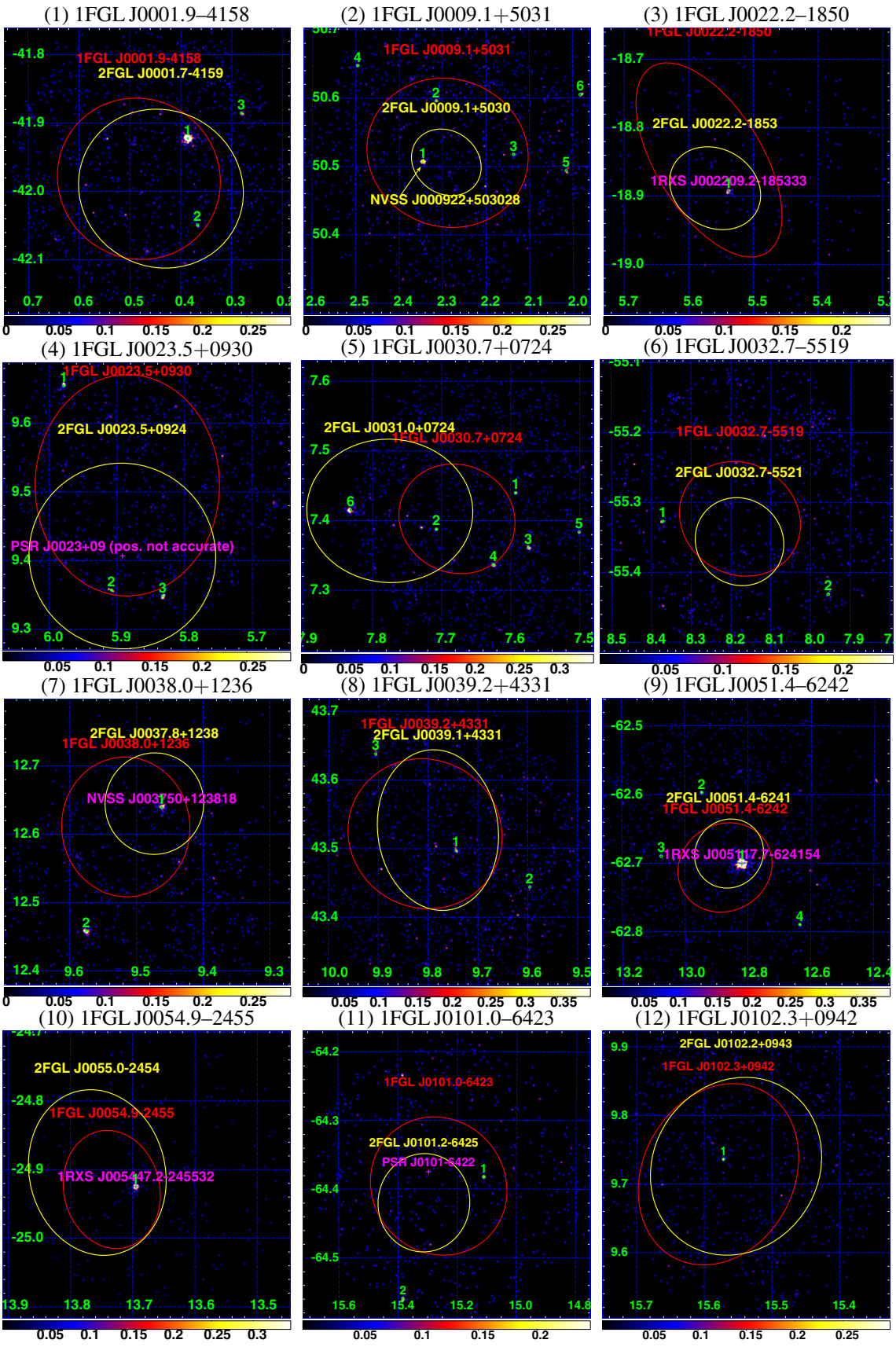

Figure 11. *Swift*/XRT images of the 134 1FGL unID catolog sources of the $25' \times 25'$ FoV. One or more sources are detected within the *Swift*/XRT FoV. Unfortunately, 2FGL error regions of some sources run off the edge of the *Swift*/XRT FoV. The signal-to-noise acceptance threshold is set to 3σ. The yellow ellipses show 95% error regions of the 2FGL catalog gamma-ray sources, and red ellipses show those of 1FGL catalog sources. If there are radio and bright X-ray sources associated with gamma-ray sources, we show those sources as magenta crosses.

(A color version of this figure is available in the online journal.)

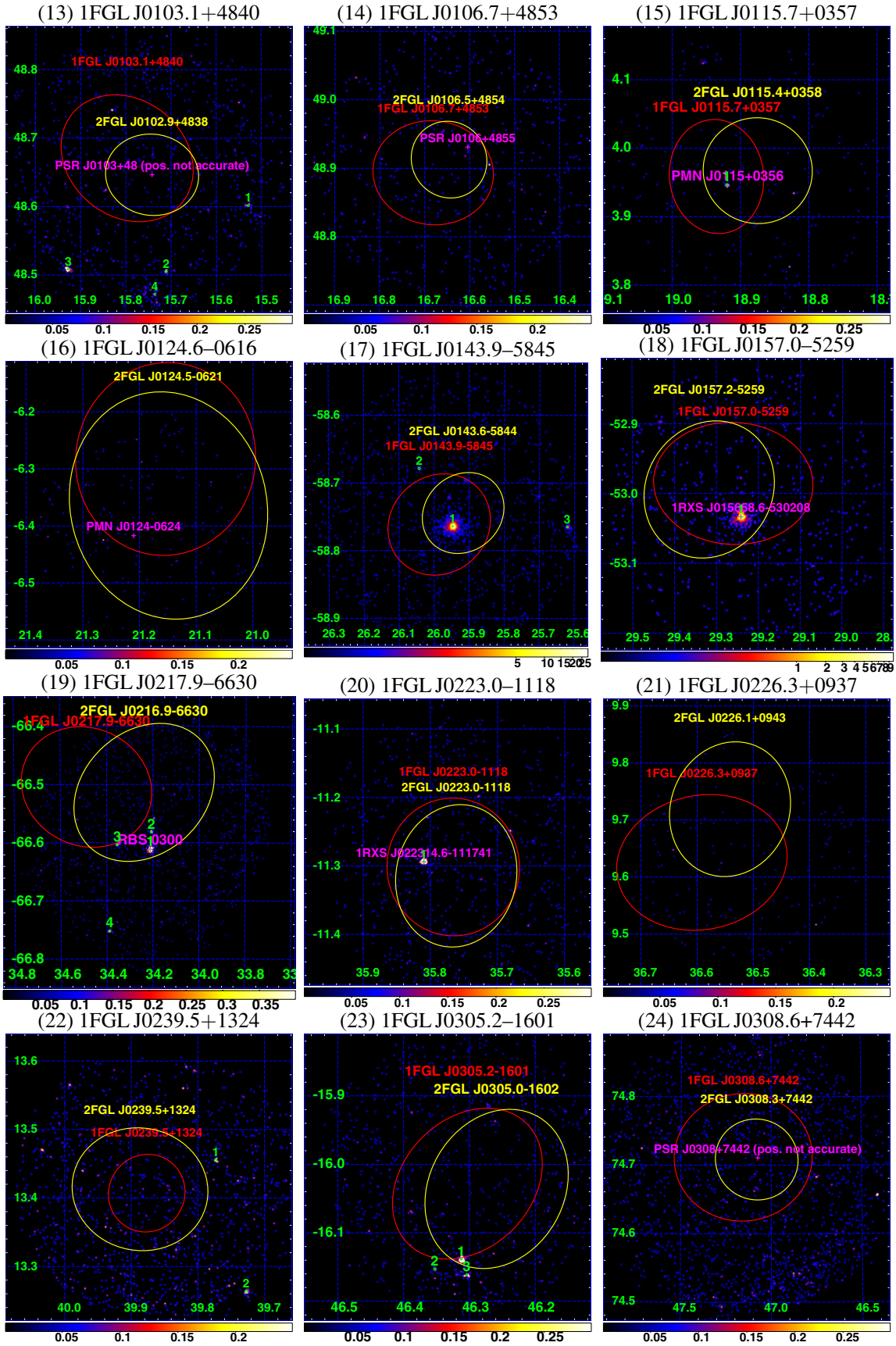

Figure 11. (Continued)

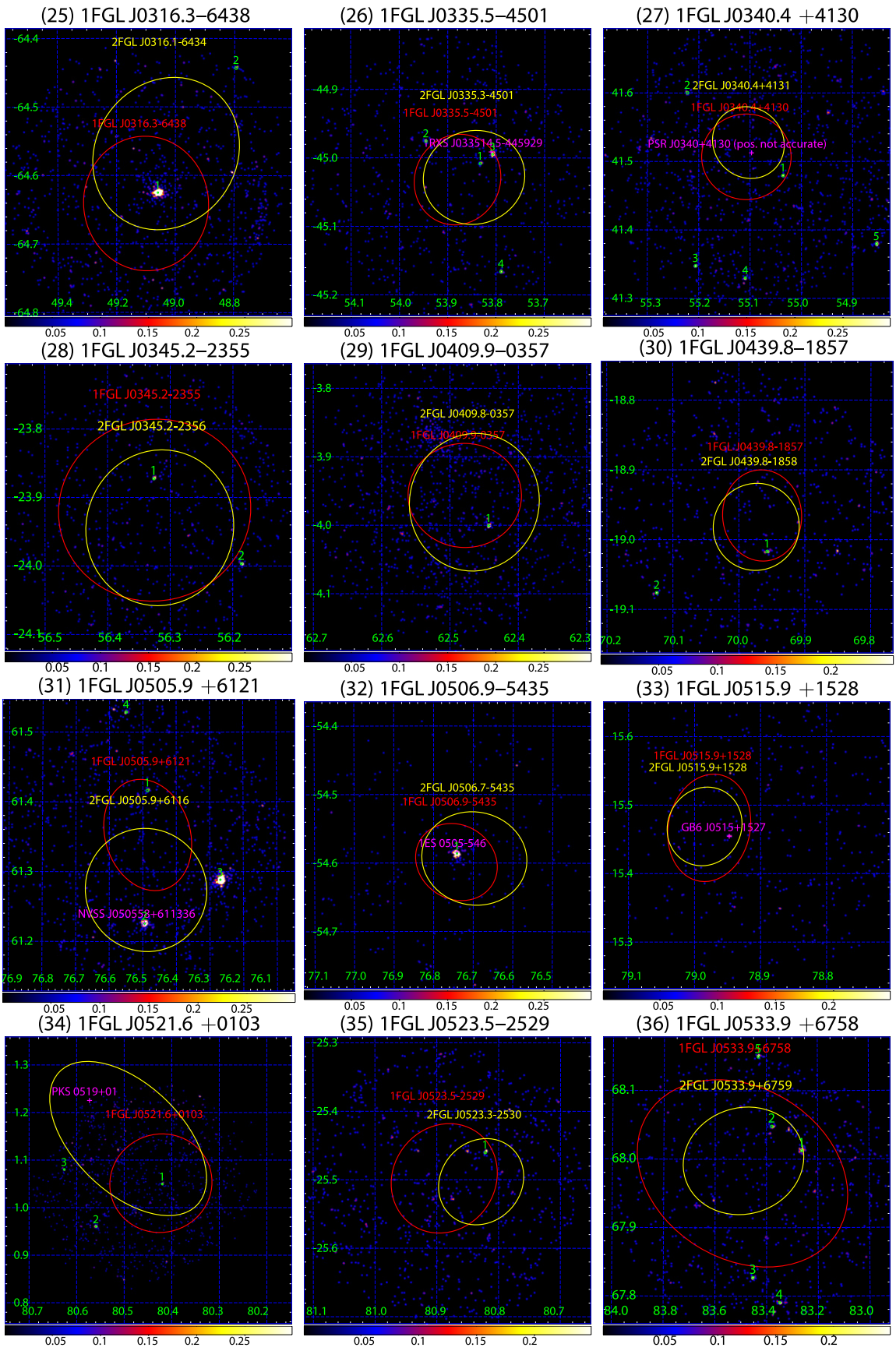

Figure 11. (Continued)

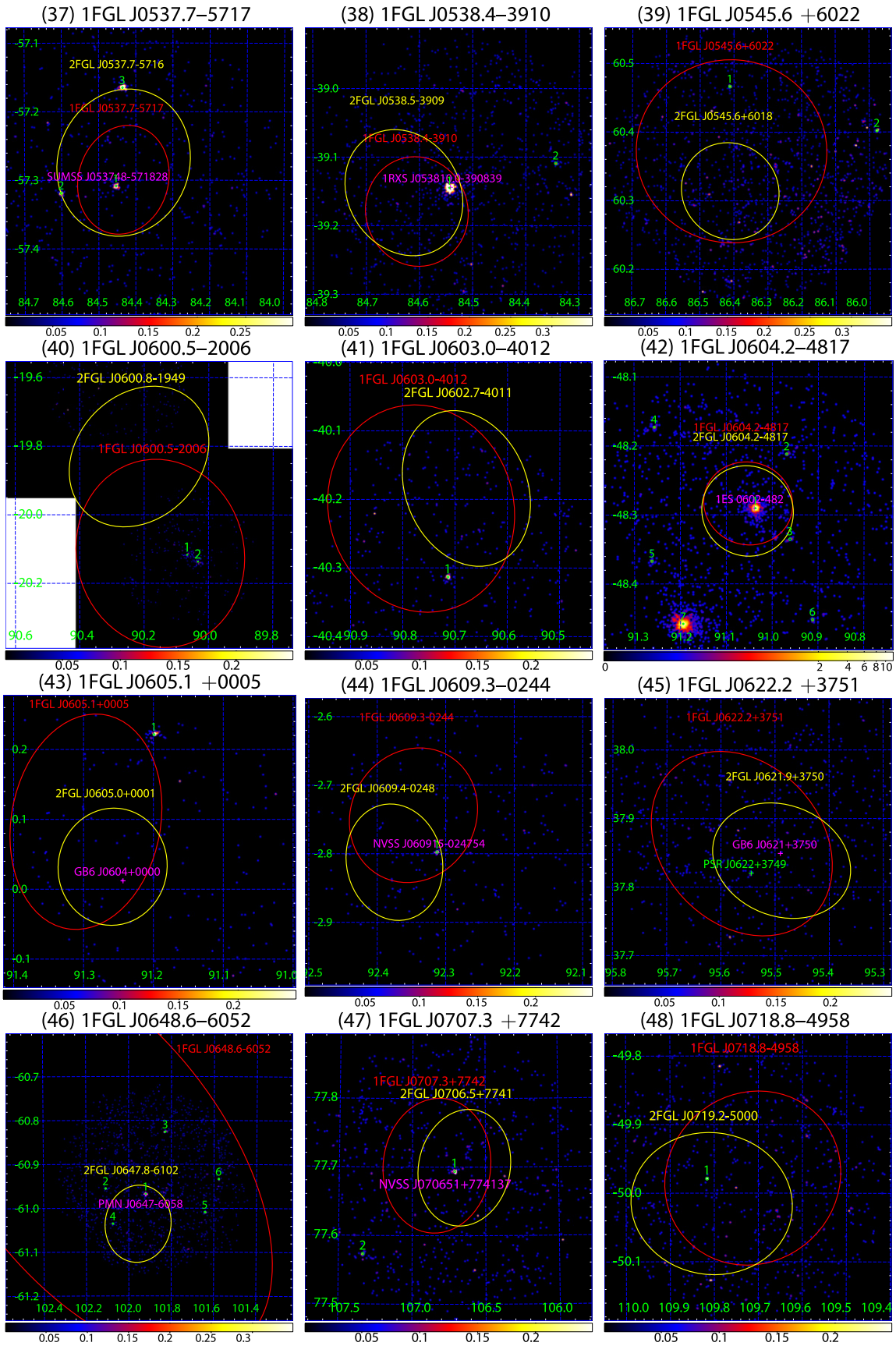

Figure 11. (Continued)

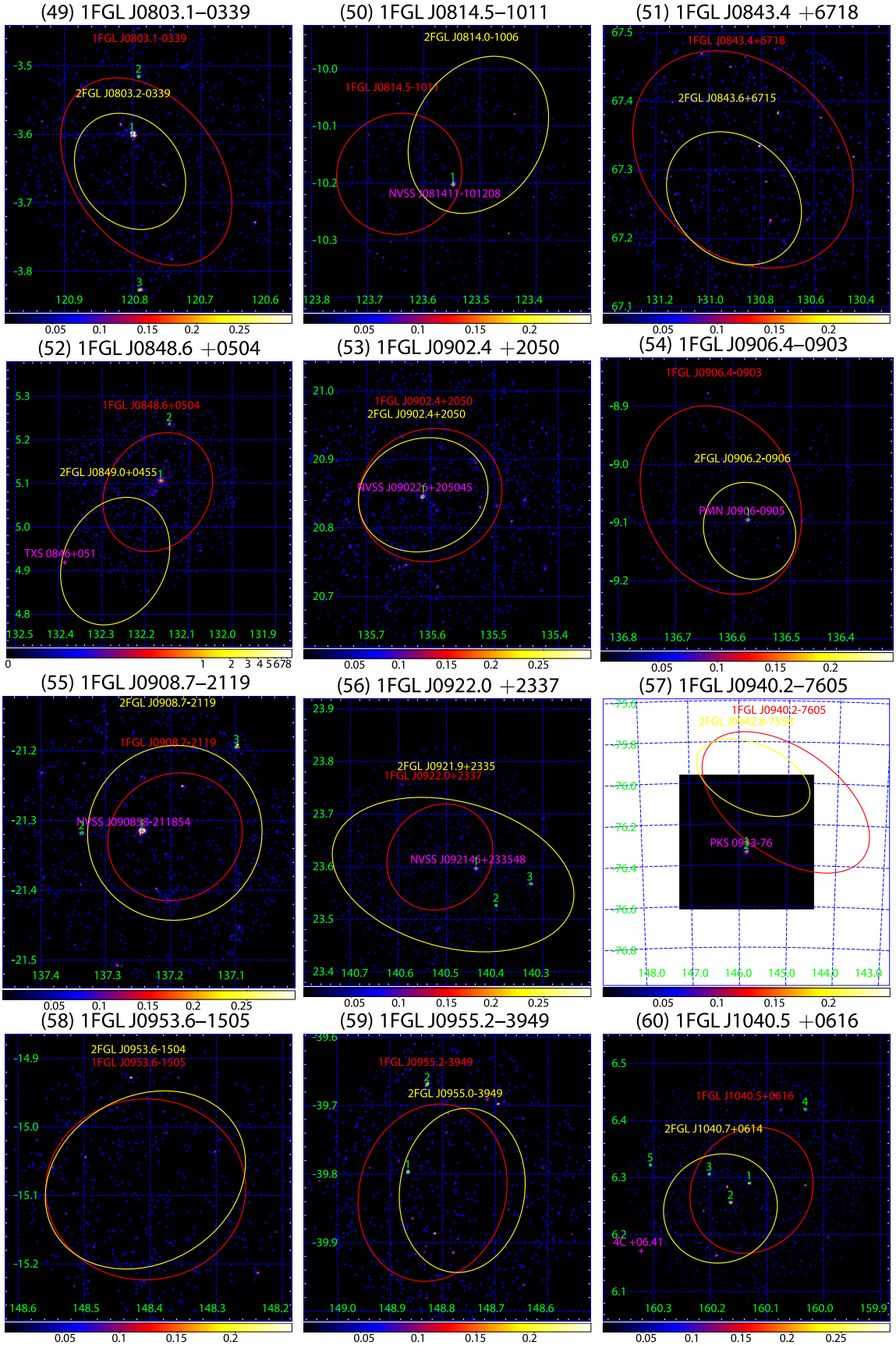

Figure 11. (Continued)

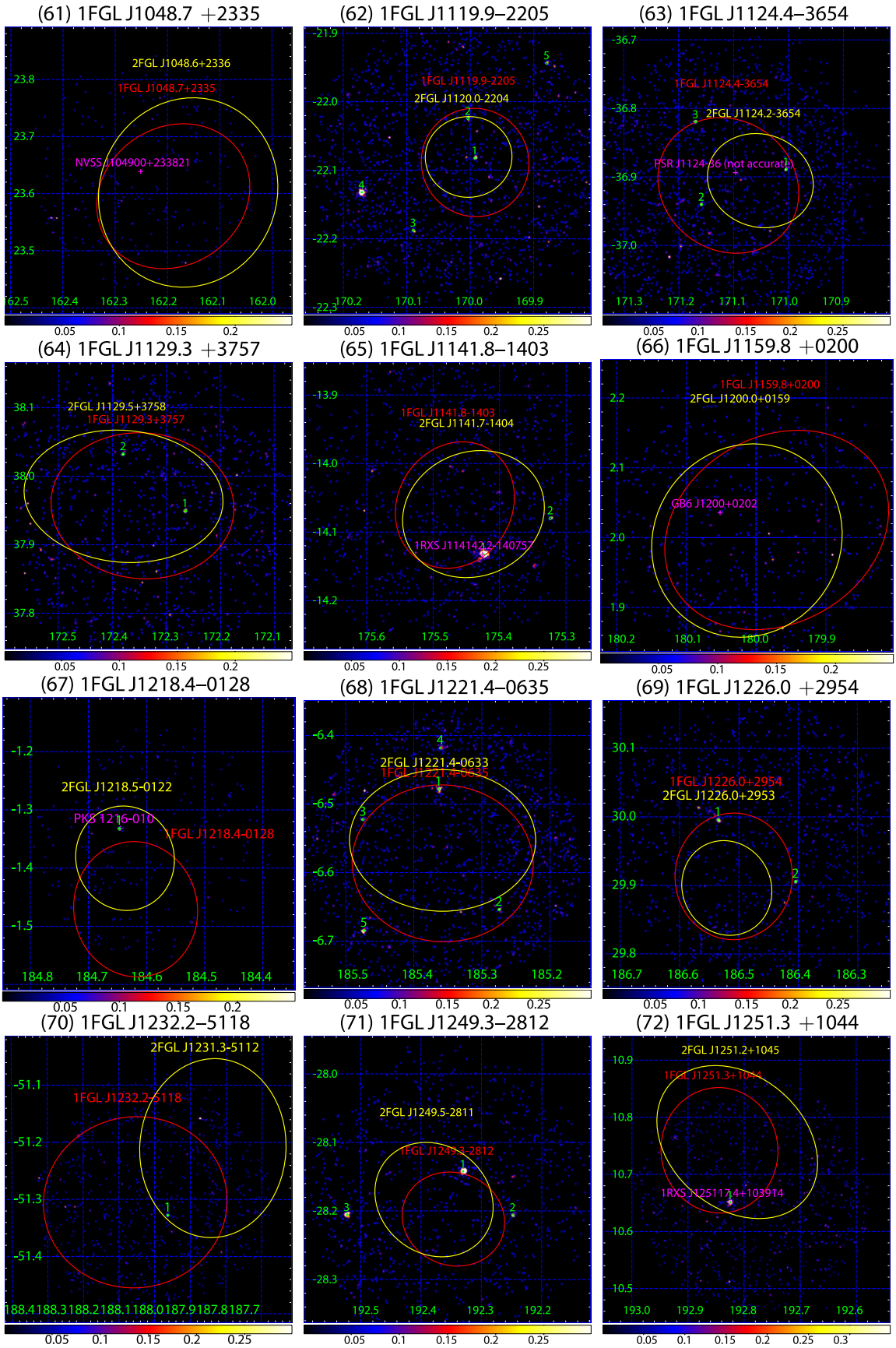

Figure 11. (Continued)

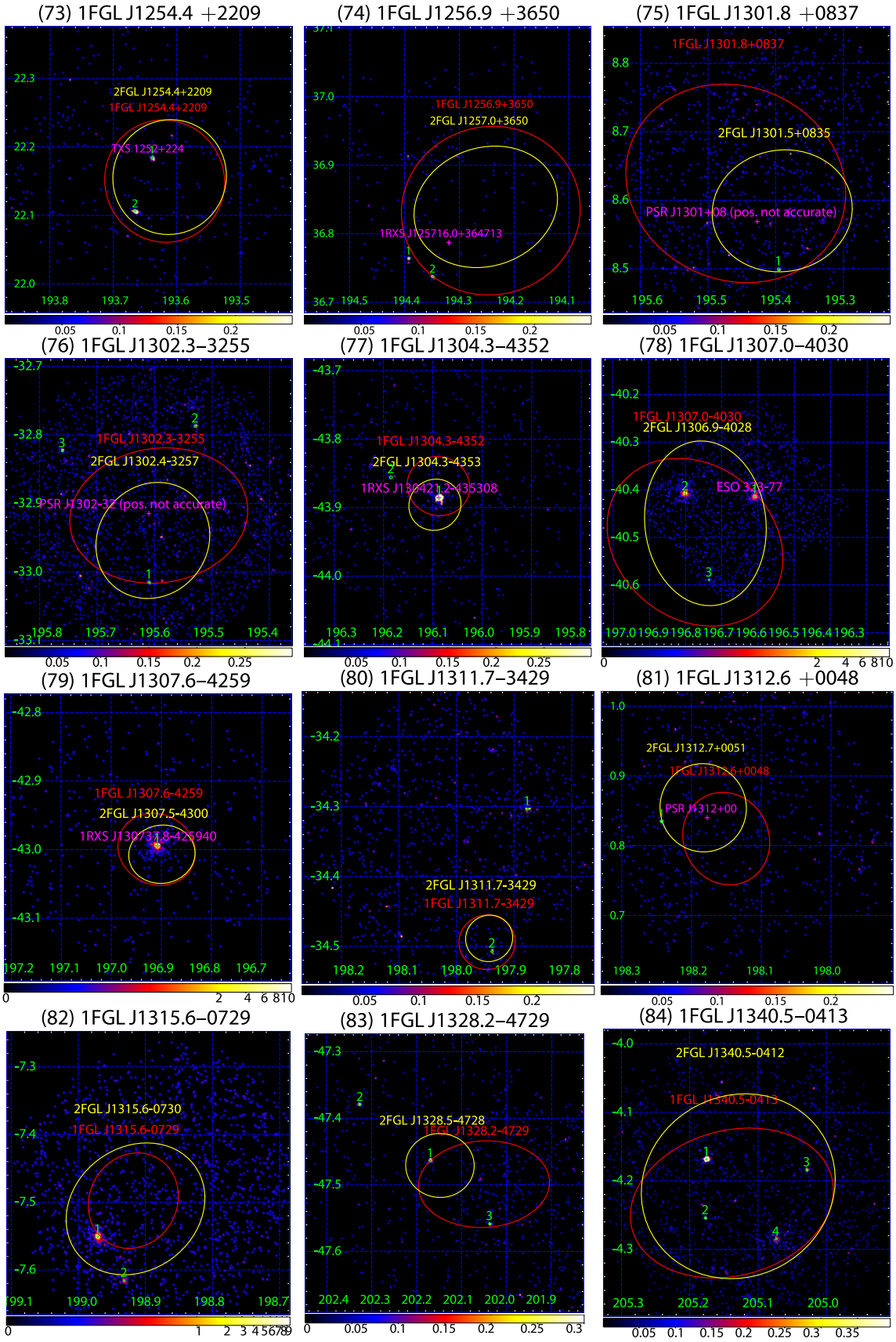

Figure 11. (Continued)

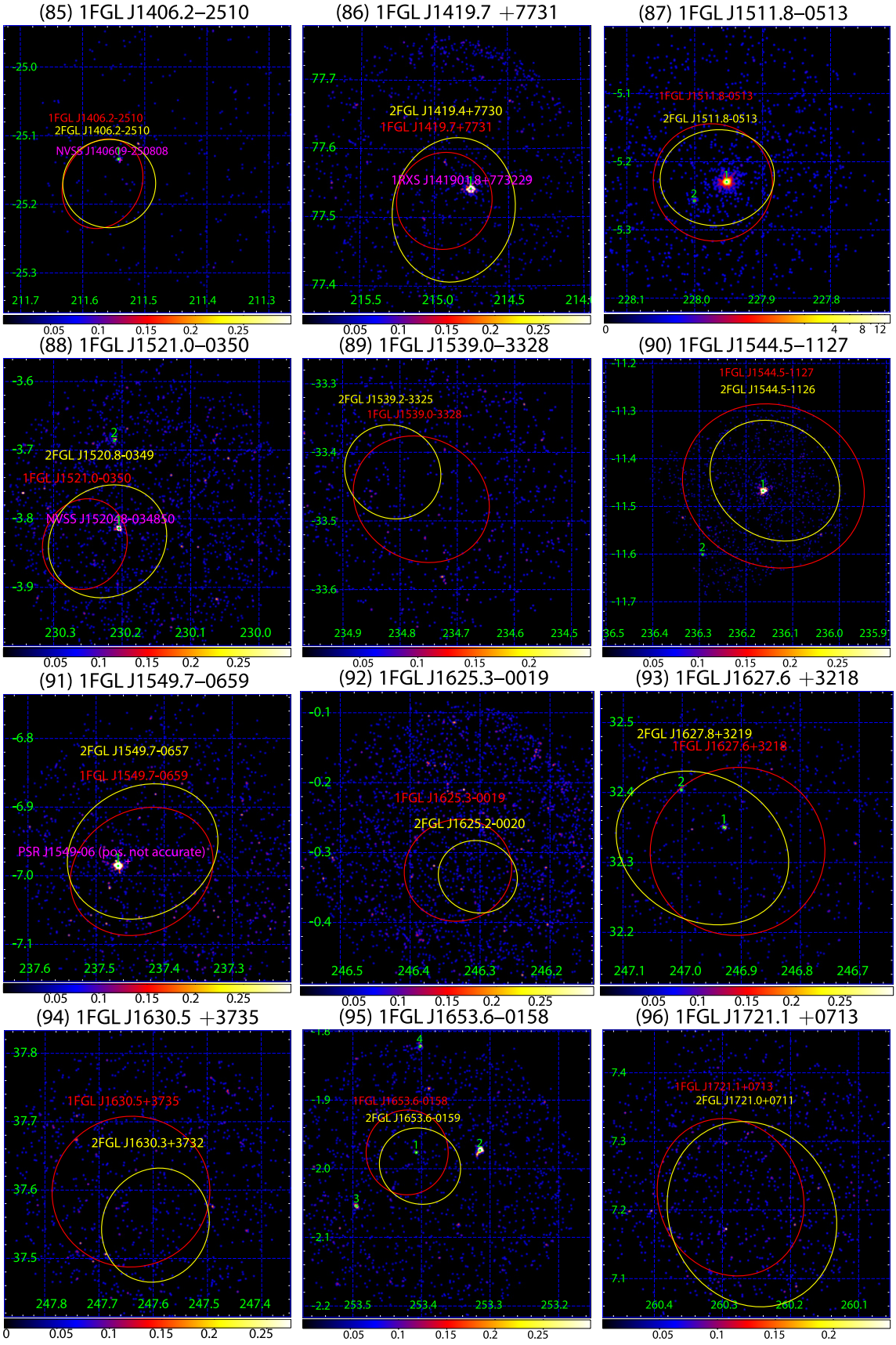

Figure 11. (Continued)

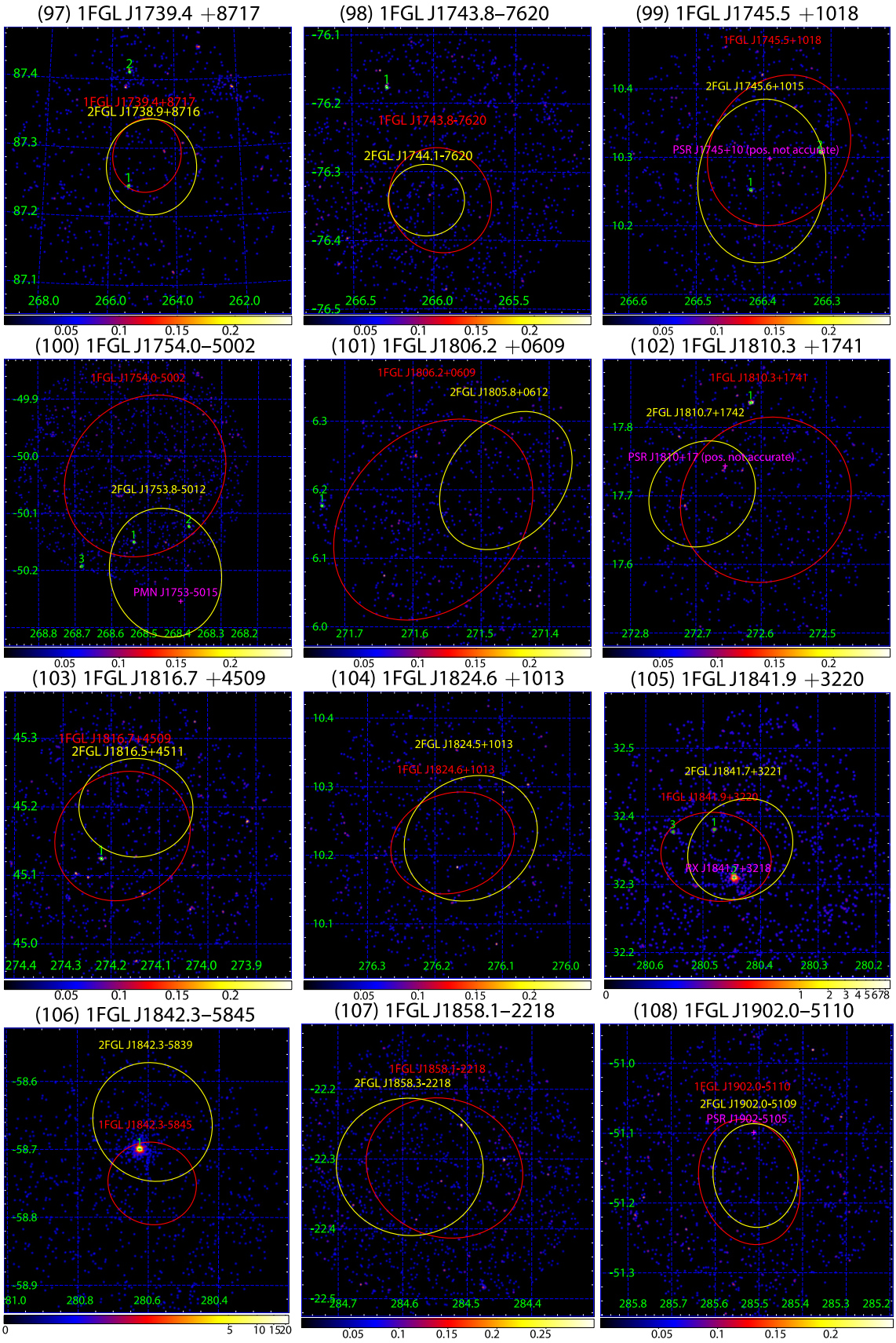

Figure 11. (Continued)

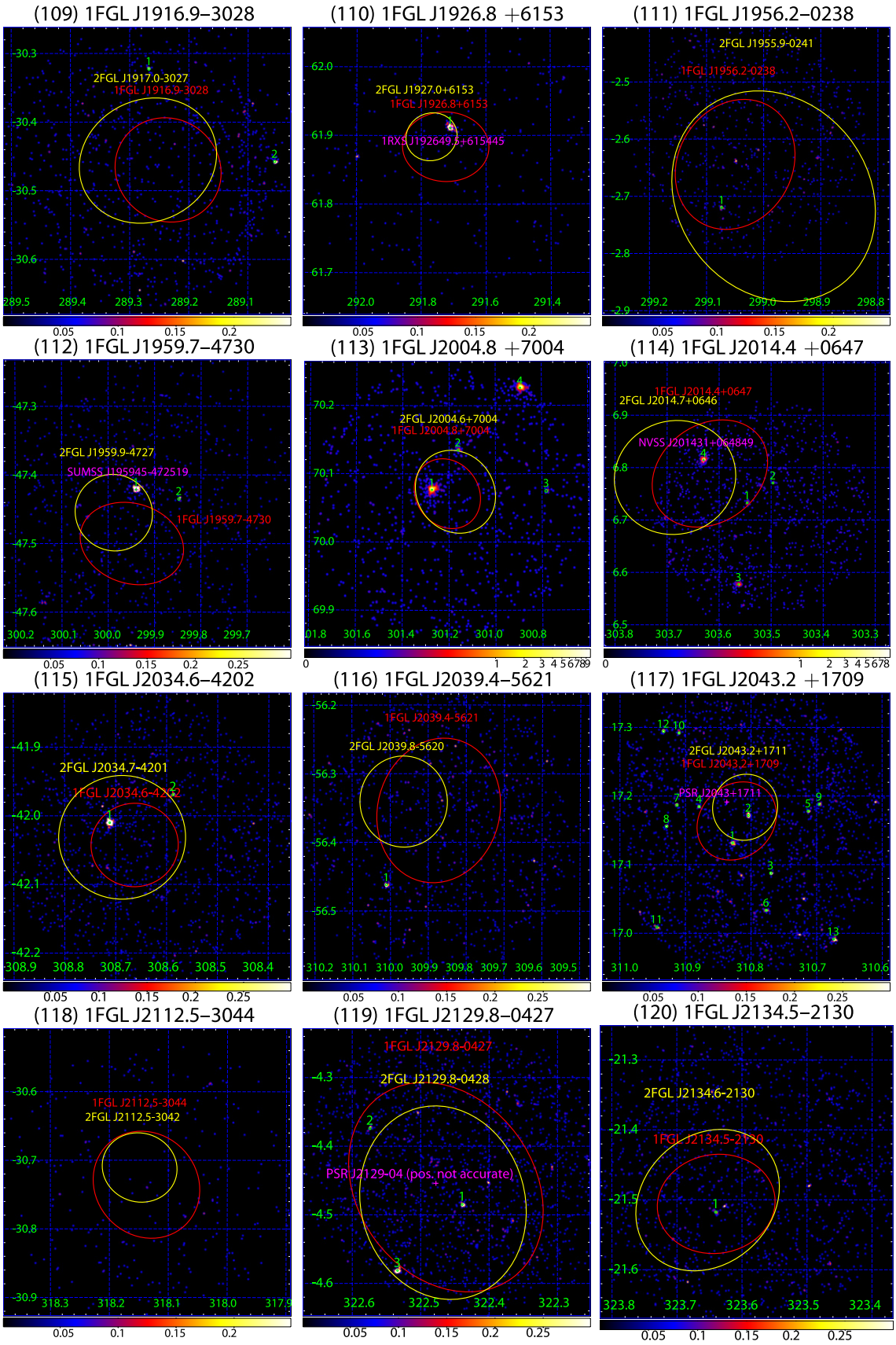

Figure 11. (Continued)

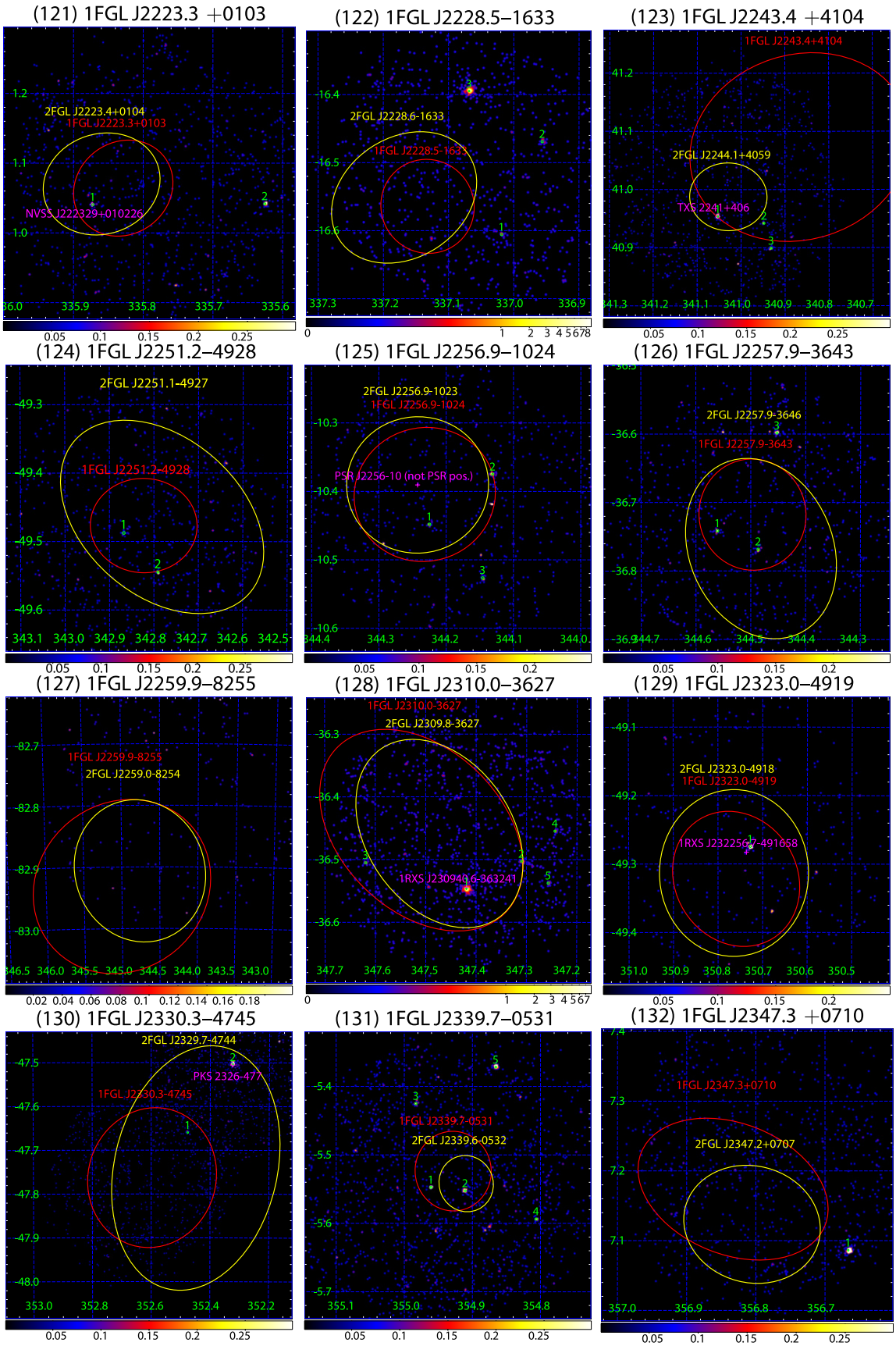

Figure 11. (Continued)

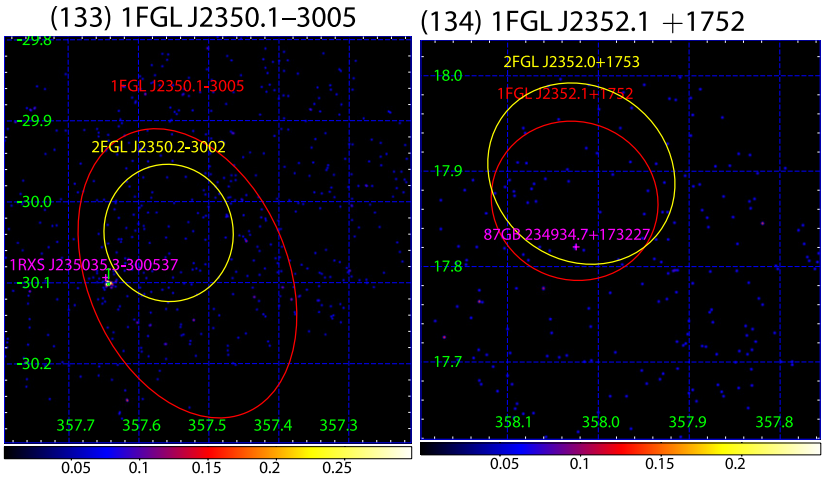

Figure 11. (Continued)

Table 5
All Radio Fluxes and *Swift*/UVOT Fluxes Plotted in SEDs (Figure 12)

	Radio (mJy)				UV (*Swift*/UVOT) (E-12 erg cm^{-2} s^{-1})					
Name	$F_{350\,\mathrm{MHz}}$	$F_{843\,\mathrm{MHz}}$	$F_{1.4\,\mathrm{GHz}}$	$F_{4.85\,\mathrm{GHz}}$	V-band	B-band	U-band	$UVW1$-band	$UVM2$-band	$UVW2$-band
J0001.9−4158_src1	...	13.2 ± 1.2	...	...	...	...	...	...	...	...
J0001.9−4158_src2	...	<5	...	...	...	...	0.131 ± 0.017	...	0.213 ± 0.030	0.152 ± 0.010
J0009.1+5031	...	...	12.1 ± 0.6	...	...	...	1.94 ± 0.06	...	...	1.61 ± 0.063
J0022.2−1850	...	...	22.4 ± 0.8	...	3.31 ± 0.33	3.39 ± 0.23	3.19 ± 0.19	2.83 ± 0.17	3.26 ± 0.21	2.51 ± 0.12
J0023.5+0930_PSRJ0023+48_src2	2.00 ± 0.01	...	...	...	...	...	...	...	...	...

(This table is available in its entirety in a machine-readable form in the online journal. A portion is shown here for guidance regarding its form and content.)

Table 6
Swift/XRT X-Ray Fluxes and 2FGL Gamma-Ray Fluxes Plotted in SEDs (Figure 12)

	X-Ray (*Swift*/XRT) (E-14 erg cm^{-2} s^{-1})						Gamma-ray (2FGL Catalog) (E-12 erg cm^{-2} s^{-1})				
Name	$F_{0.32-.64\,\mathrm{keV}}$	$F_{0.64-1.28\,\mathrm{keV}}$	$F_{1.28-2.56\,\mathrm{keV}}$	$F_{2.56-5.12\,\mathrm{keV}}$	$F_{5.12-10.24\,\mathrm{keV}}$	$U.L._{.0.5-8\,\mathrm{keV}}$	$F_{100-300\,\mathrm{MeV}}$	$F_{0.3-1\,\mathrm{GeV}}$	$F_{1-3\,\mathrm{GeV}}$	$F_{3-10\,\mathrm{GeV}}$	$F_{10-100\,\mathrm{GeV}}$
J0001.9−4158_src1	104 ± 11	86.2 ± 7.3	57.5 ± 6.4	39.2 ± 8.13	20.2 ± 12.9	...	<3.47	<1.63	<1.21	1.09 ± 0.39	<1.42
J0001.9−4158_src2	...	2.29 ± 1.29	2.96 ± 1.58	...	...	...	<3.47	<1.63	<1.21	1.09 ± 0.39	<1.42
J0009.1+5031	18.3 ± 8.45	17.0 ± 4.3	15.1 ± 3.9	6.62 ± 3.86	...	...	<2.29	2.85 ± 0.53	3.70 ± 0.55	4.10 ± 0.73	3.53 ± 1.04
J0022.2−1850	38.2 ± 17.4	37.2 ± 12.5	40.7 ± 14.5	...	...	...	<1.27	<1.34	1.27 ± 0.35	1.80 ± 0.52	3.61 ± 1.16
J0023.5+0930_PSRJ0023+48_src2	...	5.49 ± 2.27	6.68 ± 2.77	9.78 ± 5.08	24.1 ± 18.5	...	<2.70	2.64 ± 0.53	2.08 ± 0.44	<1.67	<1.27

Notes. $U.L._{.0.5-8\,\mathrm{keV}}$ shows the upper limit of X-ray fluxes. Note that all X-ray fluxes are in (E−14 erg cm^{-2} s^{-1}), while gamma-ray fluxes are in (E−12 erg cm^{-2} s^{-1}).

(This table is available in its entirety in a machine-readable form in the online journal. A portion is shown here for guidance regarding its form and content.)

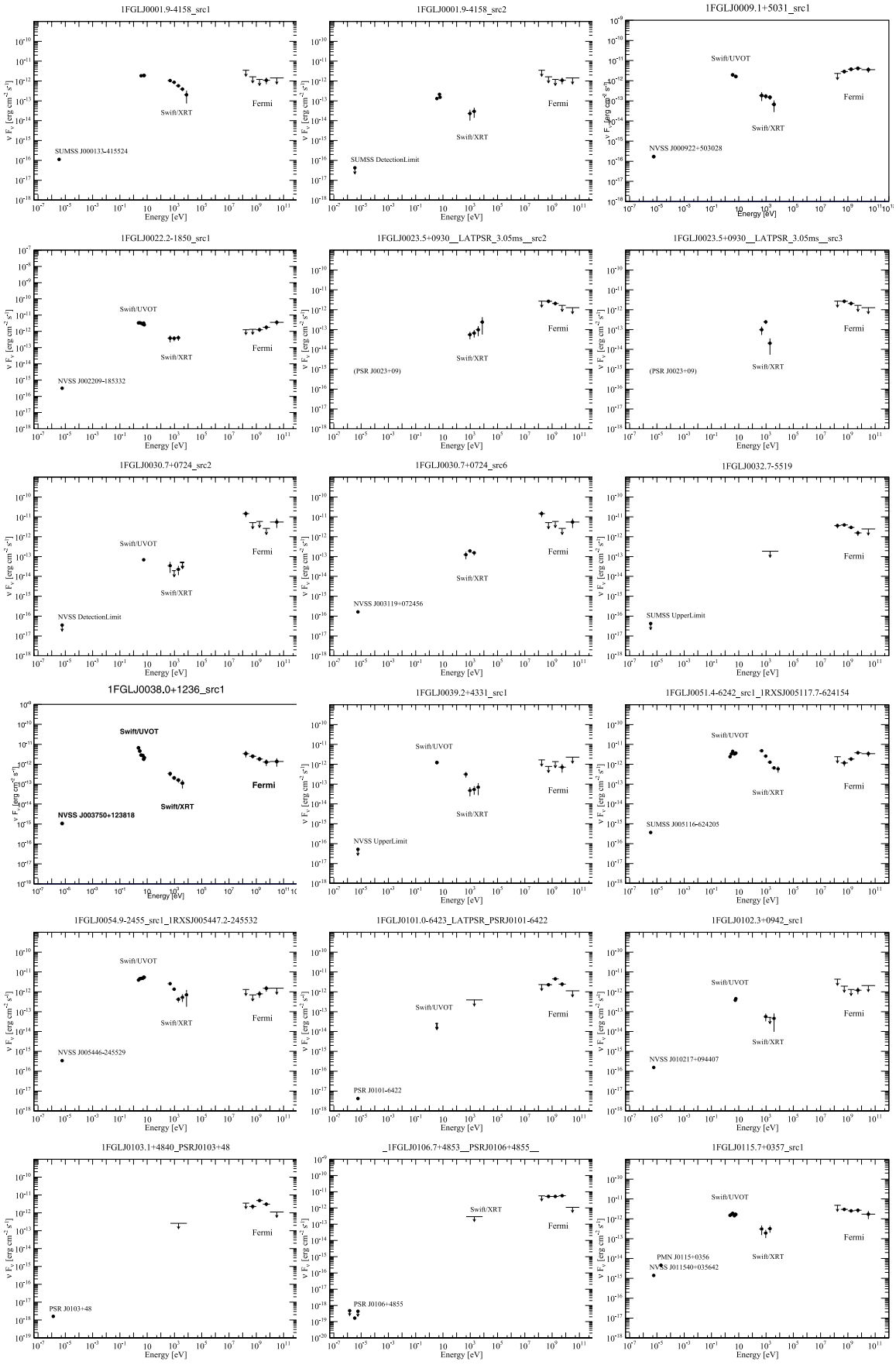

Figure 12. Broadband SEDs of the 134 1FGL unidentified sources we selected in this paper. The radio fluxes of these sources are described in Section 2.3. The X-ray fluxes for these sources are given from *Swift*/XRT analysis (see Section 2.1). Finally, the LAT fluxes of these sources are taken from the 2FGL catalog (Nolan et al. 2012). (A color version of this figure is available in the online journal.)

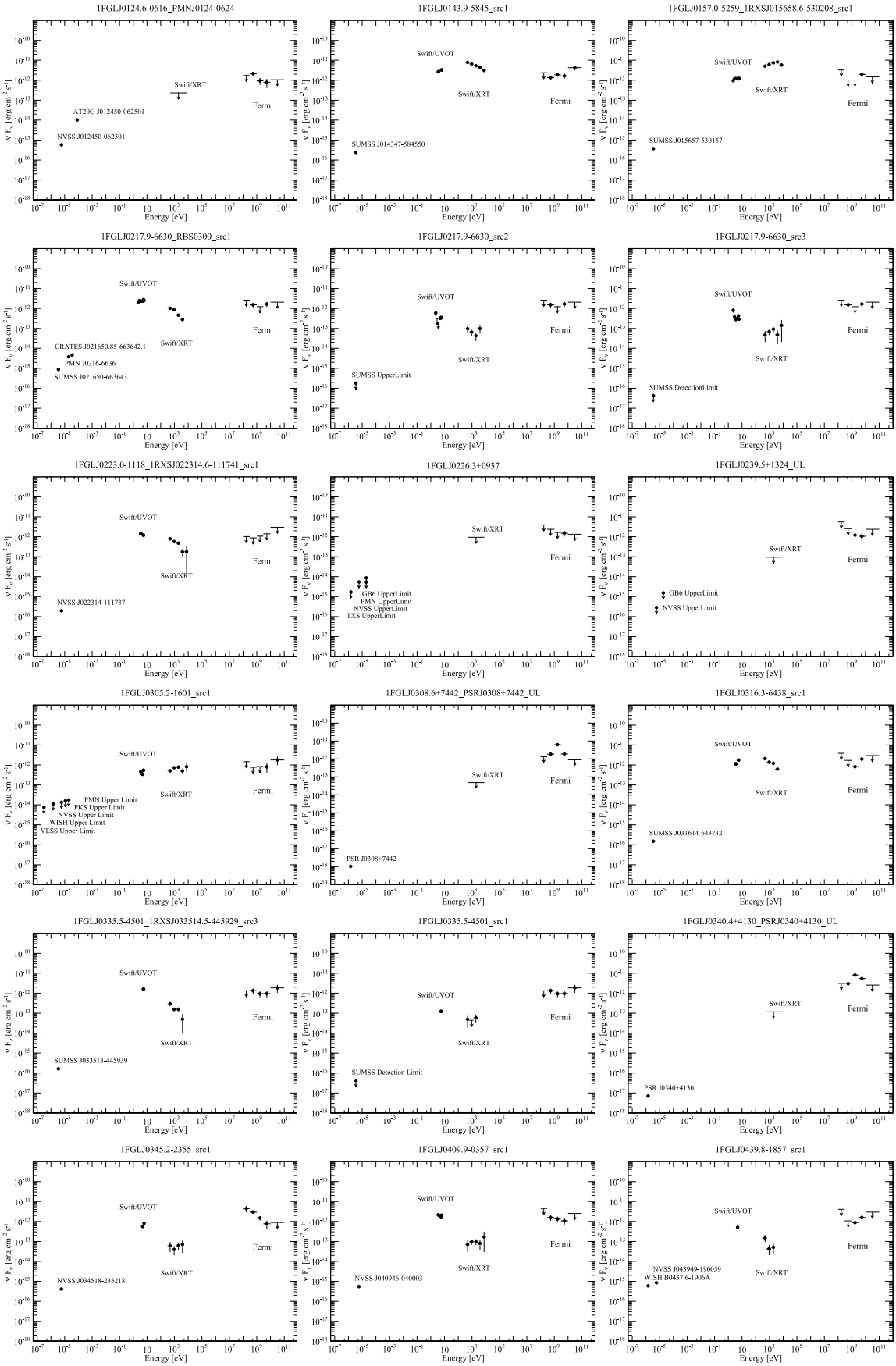

Figure 12. (Continued)

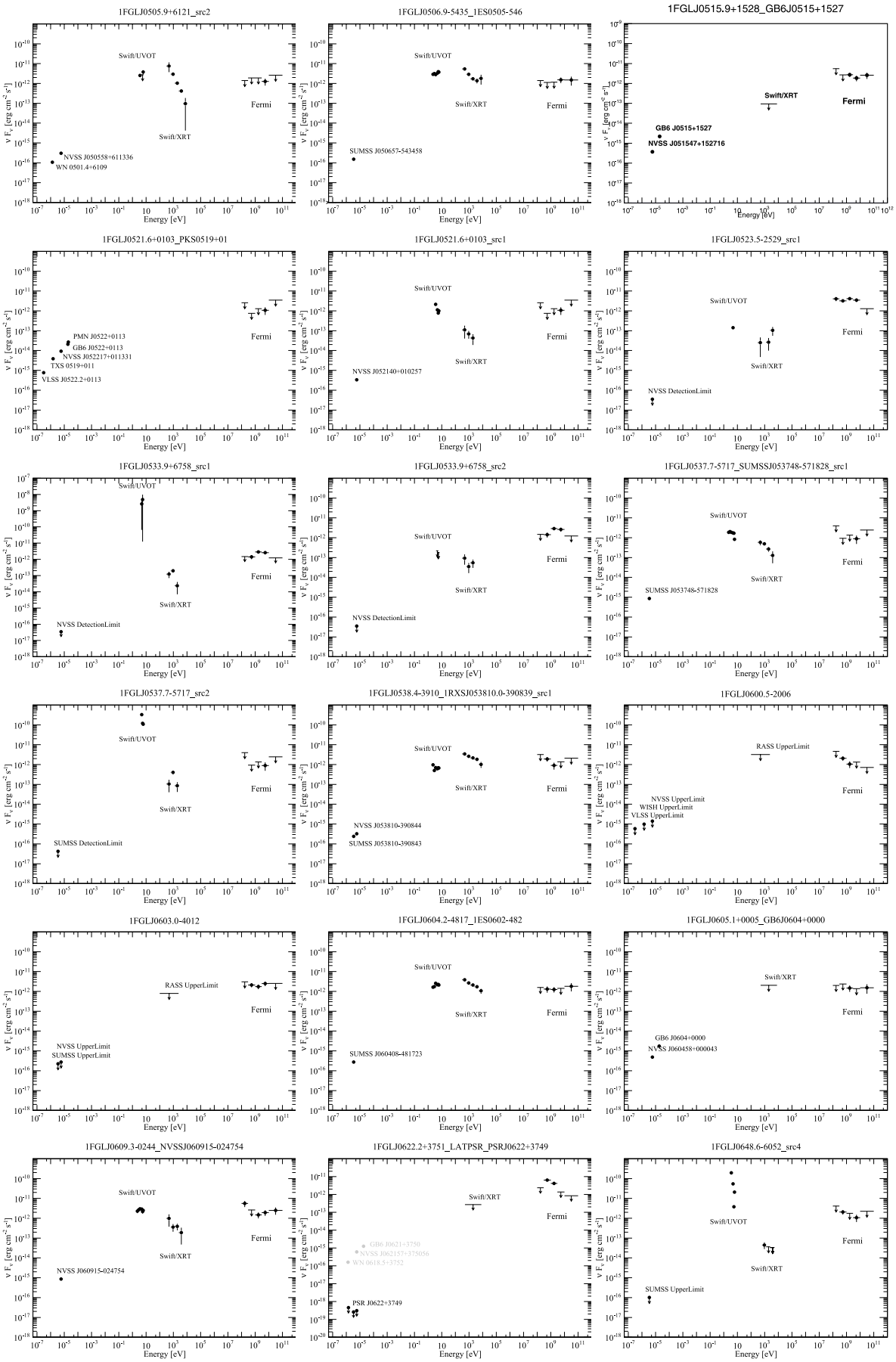

Figure 12. (Continued)

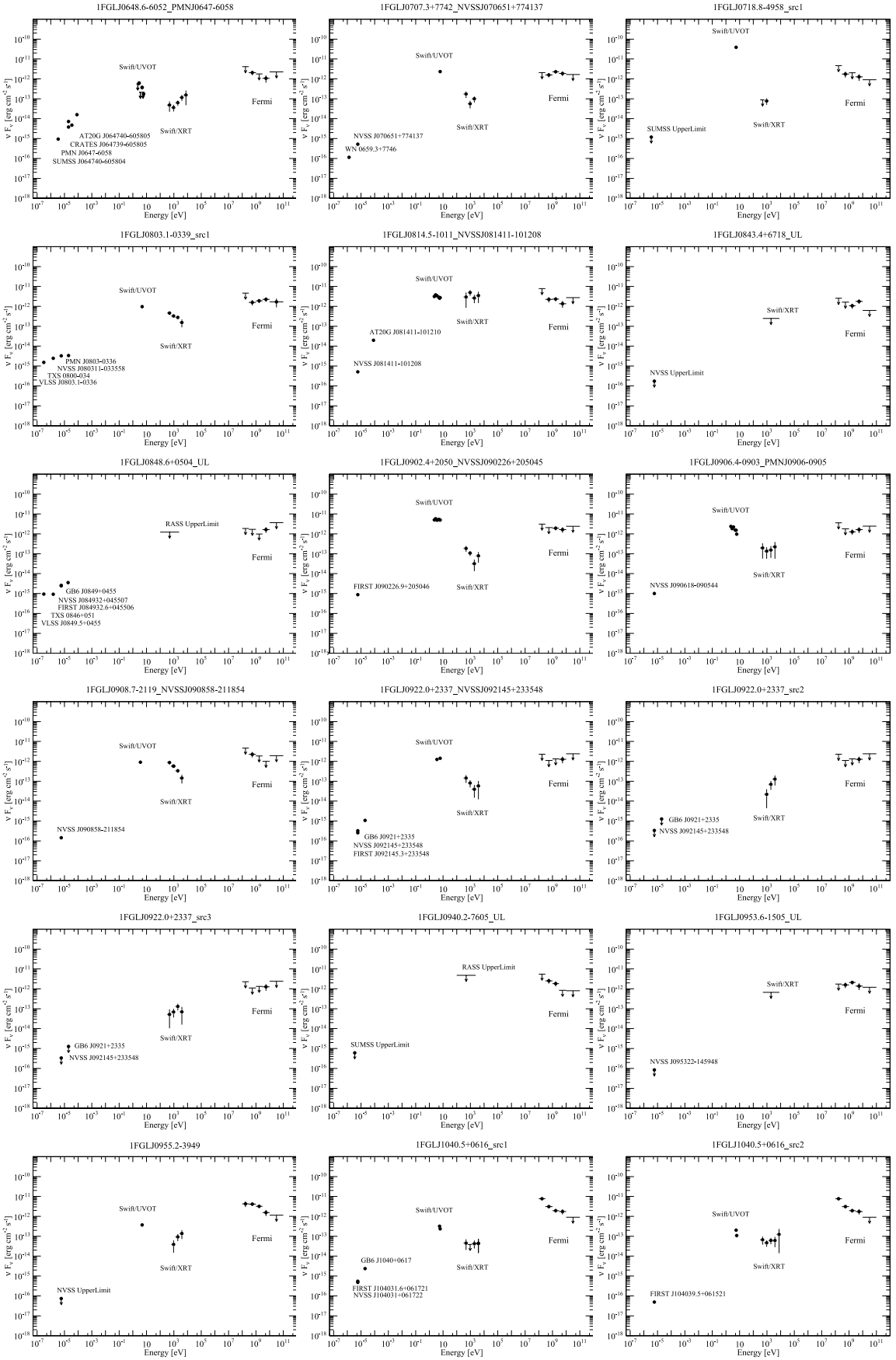

Figure 12. (Continued)

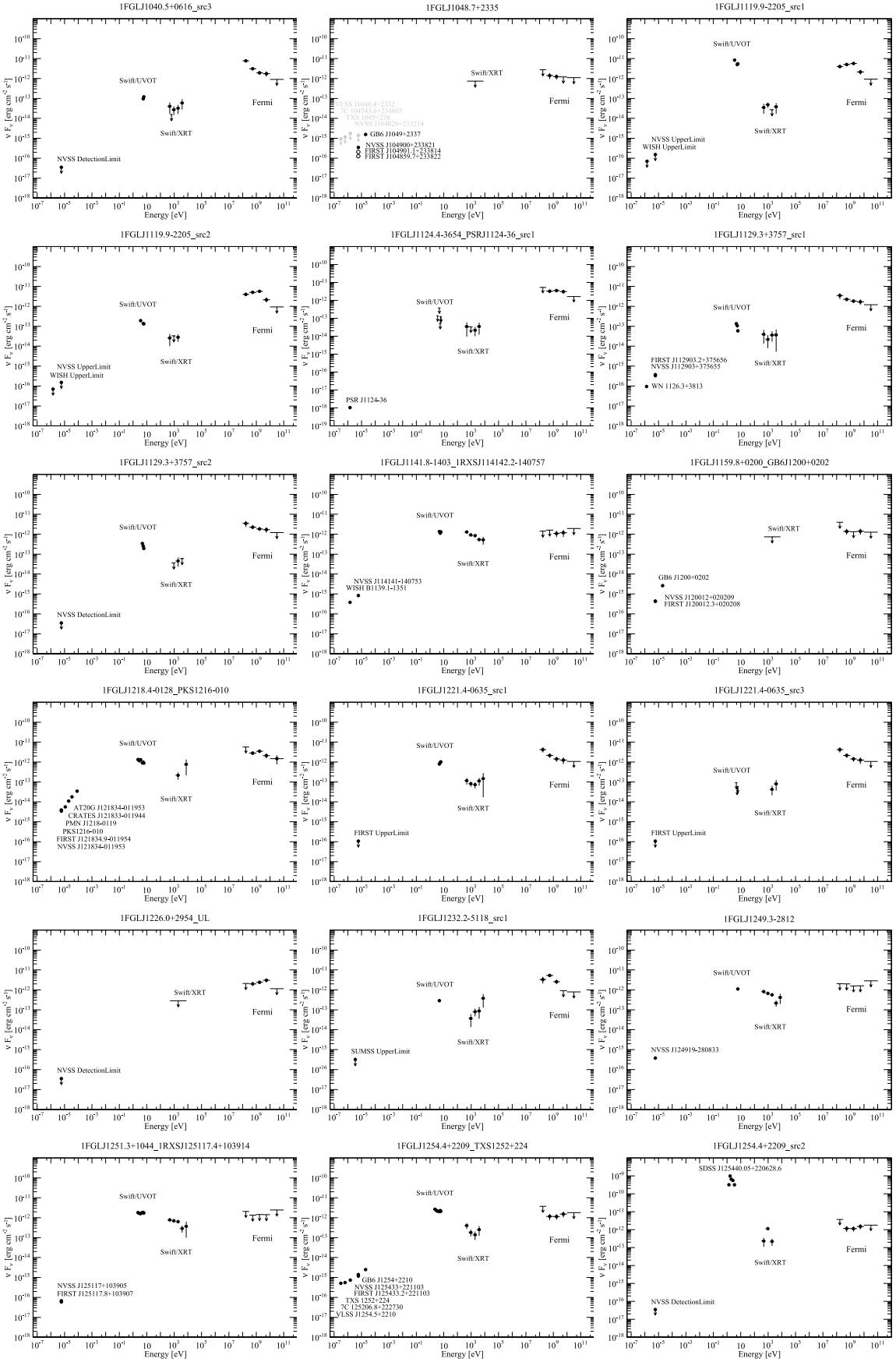

Figure 12. (Continued)

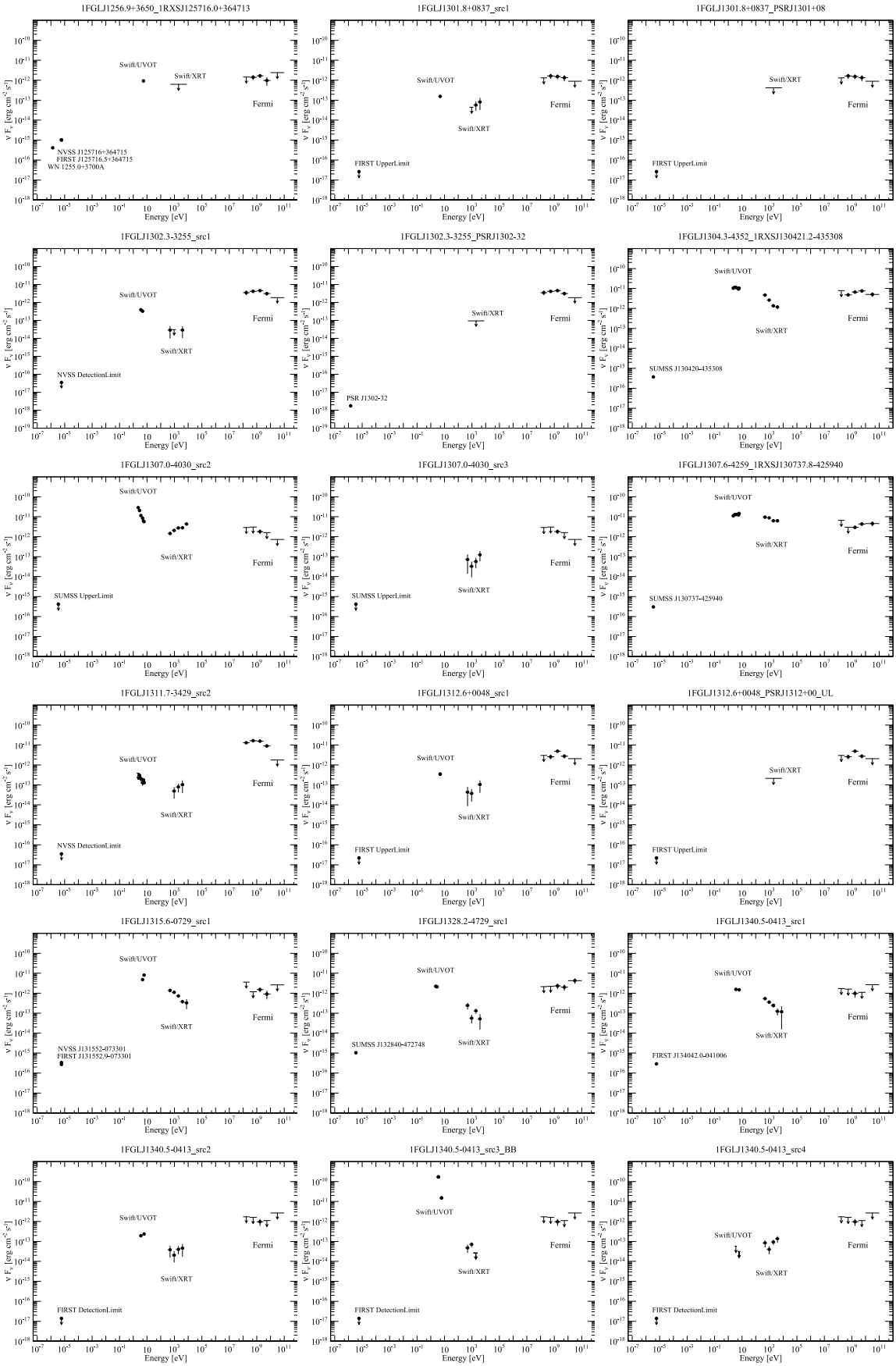

Figure 12. (Continued)

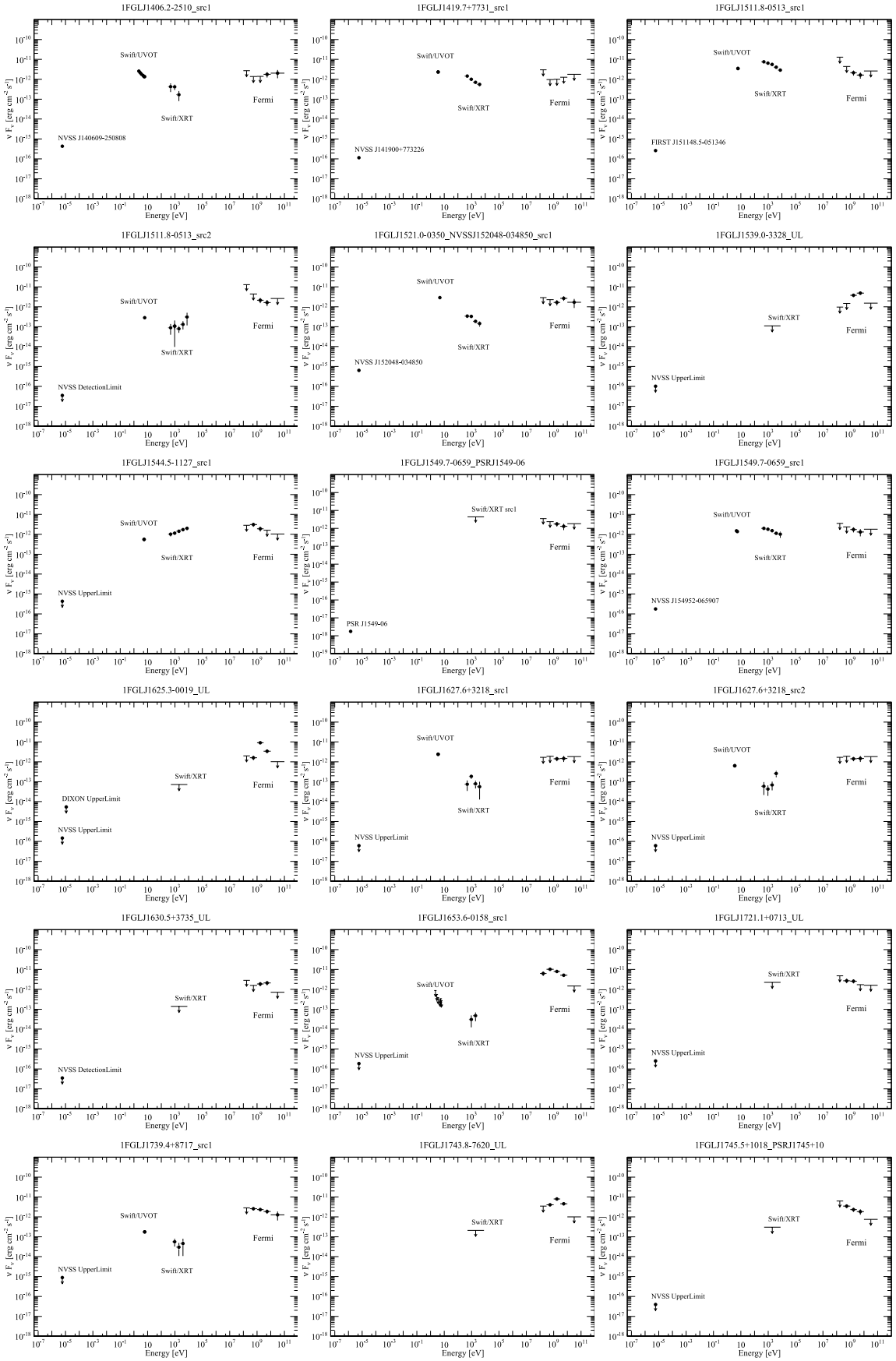

Figure 12. (Continued)

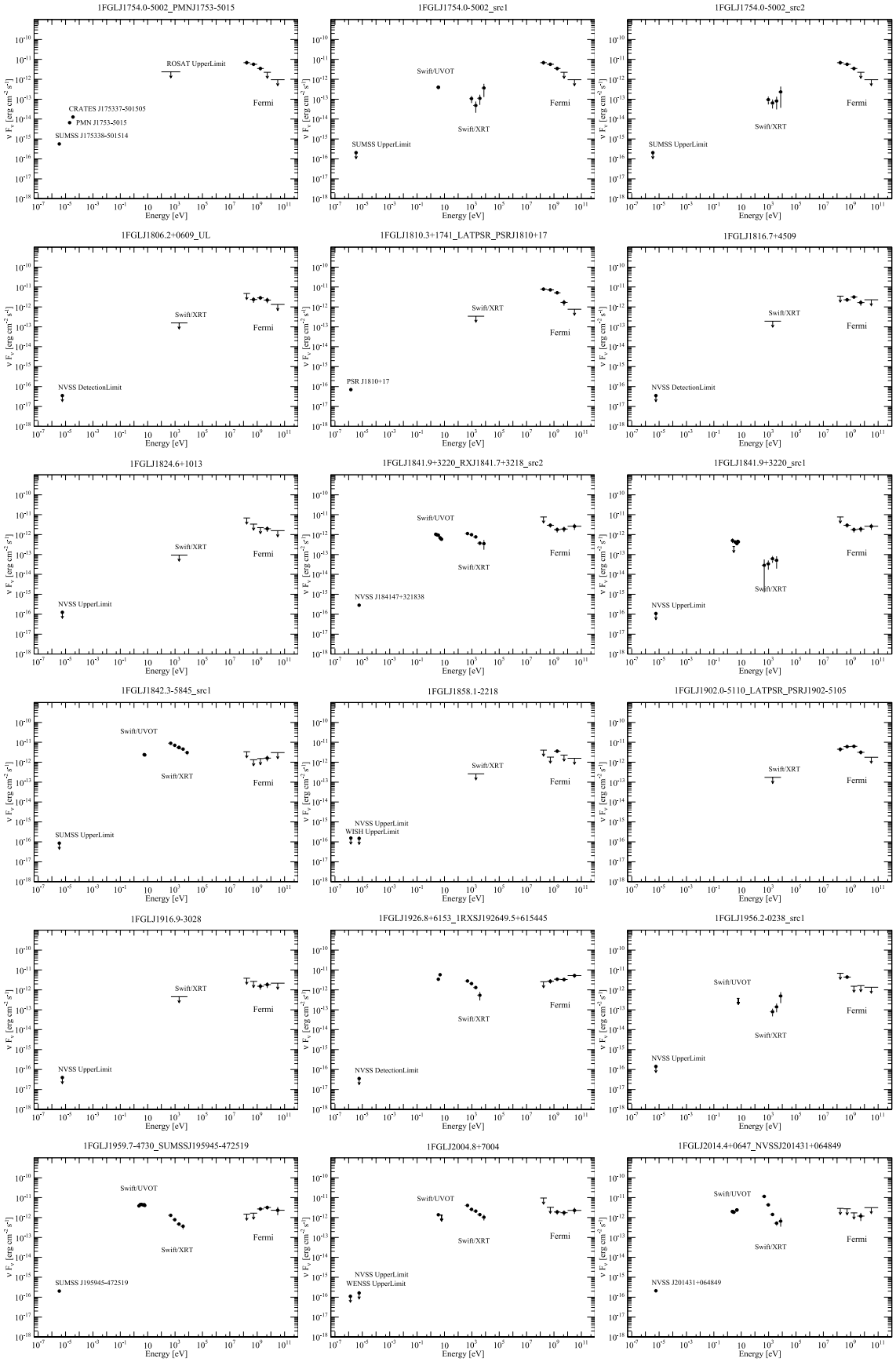

Figure 12. (Continued)

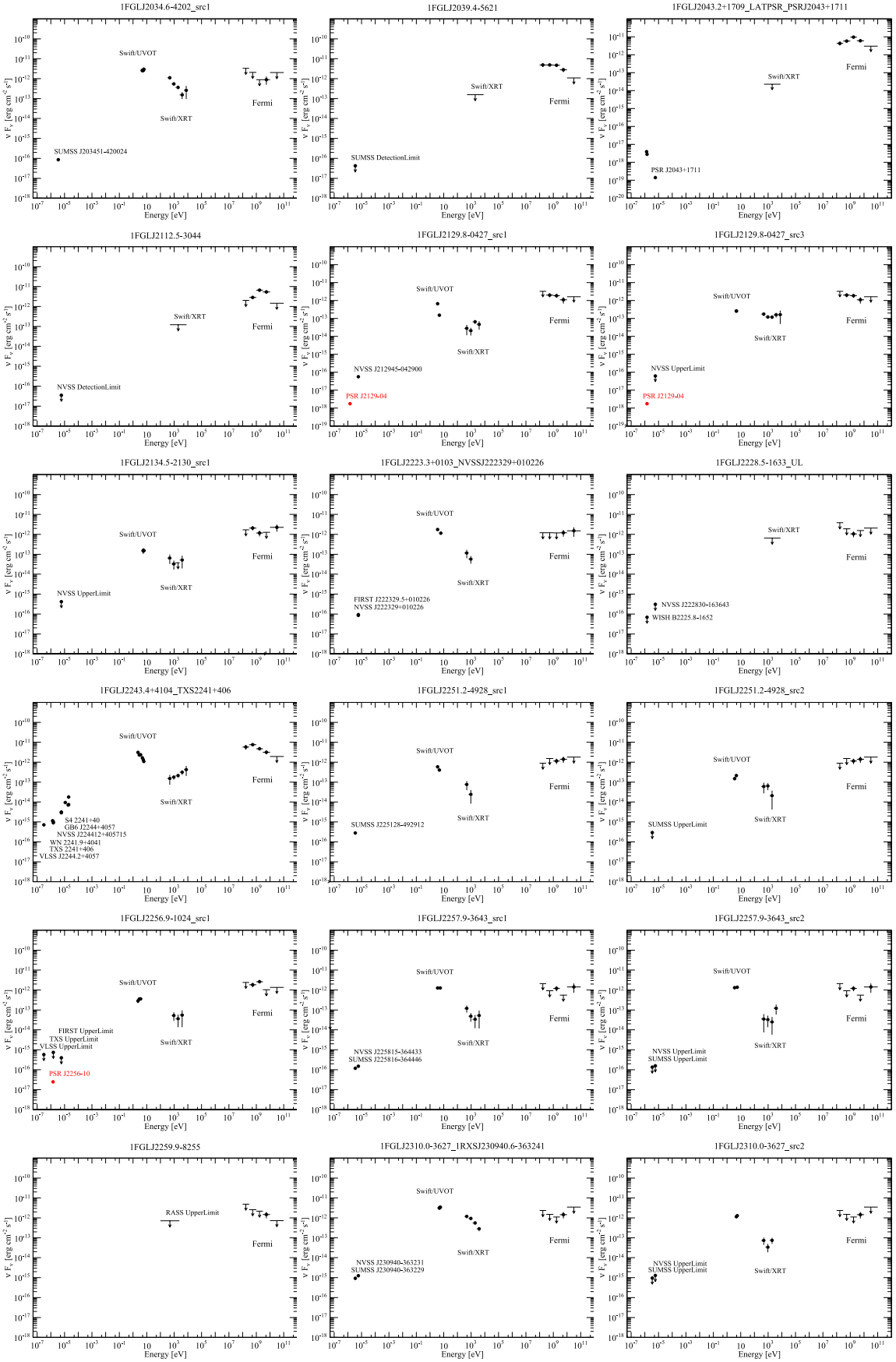

Figure 12. (Continued)

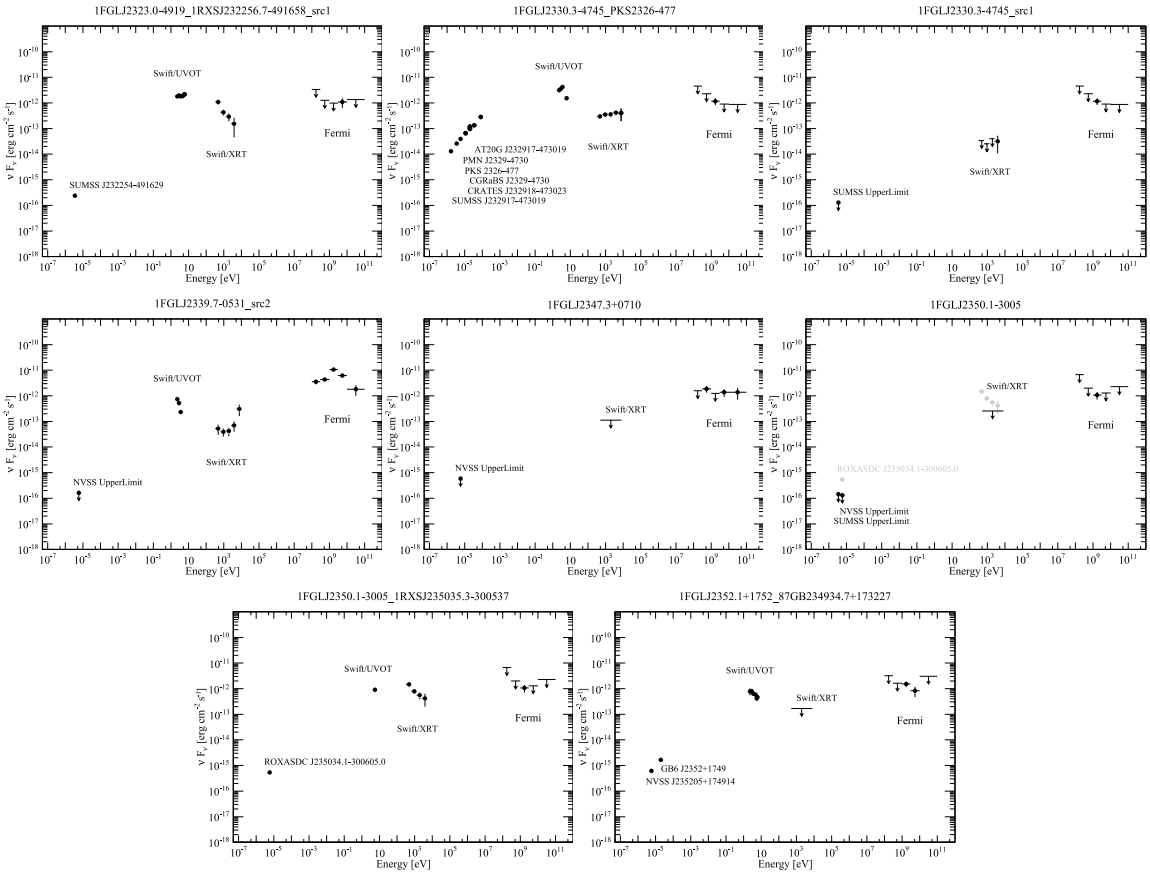

Figure 12. (Continued)

REFERENCES

Abdo, A. A., Ackermann, M., Ajello, M., et al. 2009, ApJ, 701, 123
Abdo, A. A., Ackermann, M., Ajello, M., et al. 2010a, ApJS, 187, 460
Abdo, A. A., Ackermann, M., Ajello, M., et al. 2010b, ApJS, 188, 405
Abdo, A. A., Ackermann, M., Ajello, M., et al. 2010c, ApJ, 709, 152
Abdo, A. A., Ackermann, M., Ajello, M., et al. 2010d, ApJ, 710, 92
Abdo, A. A., Ackermann, M., Ajello, M., et al. 2010e, ApJ, 714, 927
Abdo, A. A., Ackermann, M., Ajello, M., et al. 2010f, ApJ, 720, 912
Ahn, C. P., Alexandroff, R., Allende Prieto, C., et al. 2012, ApJS, 203, 21
Atwood, W. B., Abdo, A. A., Ackermann, M., et al. 2009, ApJ, 697, 1071
Burrows, D. N., Hill, J. E., & Nousek, J. A. 2005, SSRv, 120, 165
Cardelli, J. A., Clayton, G. C., & Mathis, J. S. 1998, ApJ, 345, 245
Cheung, C. C., Donato, D., Gehrels, N., Sokolovsky, K. V., & Giroletti, M. 2012, ApJ, 756, 33
Cohen, A. S., Lane, W. M., Cotton, W. D., et al. 2007, AJ, 134, 1245
Condon, J. J., Cotton, W. D., Greisen, E. W., et al. 1998, AJ, 115, 1693
Cougnard, I., Guillemot, L., Johnson, T. J., et al. 2011, ApJ, 732, 47
D'Abrusco, R., Massaro, F., & Paggi, A. 2013, ApJS, 206, 12
Day, C., et al. 1998, The ASCA Data Reduction Guide, Technical Report, v.2.0 (Greenbelt, MD: NASA GSFC)
De Breuck, C., Tang, Y., de Bruyn, A. G., Röttgering, H., & van Breugel, W. 2002, A&A, 394, 59
Dickey, J. M., & Lockman, F. J. 1990, ARA&A, 28, 215
Fossati, G., Maraschi, L., Celotti, A., Comastri, A., & Ghisellini, G. 1998, MNRAS, 299, 433
Gehrels, N., Chincarini, G., Giommi, P., et al. 2004, ApJ, 611, 1005
Ghisellini, G. 2004, NewAR, 48, 375
Gregory, P. C., Scott, W. K., Douglas, K., Condon, J. J., et al. 1996, ApJS, 103, 427
Hartman, R. C., Bertsch, D. L., Bloom, S. D., et al. 1999, ApJS, 123, 79
Ishisaki, Y., Maeda, Y., Fujimoto, R., et al. 2007, PASJ, 59, 113
Kataoka, J., Mattox, J. R., Quinn, J., et al. 1999, ApJ, 514, 138
Kataoka, J., Yatsu, Y., Kawai, N., et al. 2012, ApJ, 757, 176
Keith, M. J., Johnston, S., Ray, P. S., et al. 2011, MNRAS, 414, 1292
Kokubun, M., Makishima, K., Takahashi, T., et al. 2007, PASJ, 59, 53
Kong, A. K. H., Huang, R. H. H., Cheng, K. S., et al. 2012, ApJ, 747, 3
Koyama, K., Tsunemi, H., Dotani, T., et al. 2007, PASJ, 59, 23
Maeda, K., Kataoka, J., Nakamori, T., et al. 2011, ApJ, 729, 103
Massaro, F., D'Abrusco, R., Paggi, A., et al. 2013, ApJS, 206, 13
Mauch, T., Murphy, T., Buttery, H. J., et al. 2003, MNRAS, 342, 1117
Mitsuda, K., Bautz, M., Inoue, H., et al. 2007, PASJ, 59, 1
Murphy, T., Sadler, E. M., Ekers, R. D., et al. 2010, MNRAS, 402, 2403
Nolan, P., Abdo, A. A., Ackermann, M., et al. 2012, ApJS, 199, 31
Ransom, S. M., Ray, P. S., Camilo, F., et al. 2011, ApJ, 727, 16
Romani, R. W. 2012, ApJ, 754, 25
Romani, R. W., & Shaw, M. S. 2011, ApJ, 743, 26
Roming, P. W. A., Kennedy, T. E., Mason, K. O., et al. 2005, SSRv, 120, 95
Serlemitsos, P. J., Soong, Y., Chan, K.-W., et al. 2007, PASJ, 59, 9
Takahashi, T., Abe, K., Endo, M., et al. 2007, PASJ, 59, 35
Takahashi, Y., Kataoka, J., Nakamori, T., et al. 2012, ApJ, 747, 64
Tawa, N., Hayashida, K., Nagai, M., et al. 2008, PASJ, 60, 11
Theureau, G., Parent, D., Cognard, I., et al. 2011, A&A, 525, 94
Voges, W., Aschenbach, B., Boller, Th., et al. 1999, A&A, 349, 389
White, R. L., Becker, R. H., Helfand, D. J., & Gregg, M. D. 1997, ApJ, 475, 479
Wright, A. E., Griffith, M. R., et al. 1996, ApJS, 103, 145
Wright, E. L., Eisenhardt, P. R. M., Mainzer, A. K., et al. 2010, AJ, 140, 1868